Department of Physics and Astronomy

University of Heidelberg

Master thesis

in Physics

submitted by

Adrian Herkert

born in Mosbach

2015

Gaseous Helium Cooling of a Thin Silicon Pixel Detector for the Mu3e Experiment

This Master thesis has been carried out by Adrian Herkert

at the

Institute of Physics

under the supervision of

Prof. Dr. André Schöning

Abstract

The Mu3e experiment will search for the lepton flavor violating decay $\mu^+ \to e^+e^+e^-$, which is suppressed to unobservable levels in the Standard Model. A signal would be a clear sign of New Physics.
The goal of the Mu3e experiment is to reach a sensitivity for the branching ratio of 10^{-16}. In order to sufficiently suppress backgrounds, the Mu3e detector is required to provide high momentum, vertex, and time resolution. The decay electrons (positrons) have energies $\lesssim 53\,\mathrm{MeV}$, because the muons decay at rest on a target. In this energy regime, multiple Coulomb scattering in the detector material limits the momentum and vertex resolution. Therefore, the Mu3e detector has to be optimized for a low material budget in its active parts. In order to meet this requirement and, at the same time, to be able to operate at high muon decay rates, the main component of the detector, a pixel tracker, is designed to consist of High-Voltage Monolithic Active Pixel Sensors (HV-MAPS). HV-MAPS include fast readout electronics and can be thinned to 50 µm. Their power consumption is expected to be approximately $250\,\mathrm{mW/cm^2}$. The cooling system must be capable of keeping the temperature of the pixel sensors at a reasonable level (between 0 and 70 °C) while meeting the requirement of a low material budget. It is planned to cool the tracking detector with gaseous helium.
In the context of this thesis, gaseous helium cooling of the Mu3e pixel detector was investigated experimetnally, using heatable detector models, and with the help of computational fluid dynamics (CFD) simulations. The results of both methods were found to be consistent and suggest that the proposed cooling concept is suitable for the Mu3e experiment.

Zusammenfassung

Das Mu3e-Experiment wird nach dem Zerfall $\mu^+ \to e^+e^+e^-$ suchen, welcher die Leptonzahlerhaltung verletzt und nach dem Standardmodell nicht beobachtbar ist. Ein Signal wäre ein klares Zeichen für Neue Physik jenseits des Standardmodells.
Es wird mit dem Mu3e-Experiment eine Sensitivität für das Verzweigungsverhältnis von 10^{-16} angestrebt. Um den Untergrund ausreichend zu unterdrücken, muss der Mu3e-Detektor hohe Impuls-, Vertex- und Zeitauflösung besitzen. Die Energie der Zerfallselektronen(-positronen) beträgt $E \lesssim 53\,\mathrm{MeV}$. In diesem Energiebereich beschränkt Mehrfachsreuung im Detektormaterial die Impuls- und Vertexauflösung. Daher wird der Detektor auf ein geringes Materialbudget in den aktiven Bereichen optimiert. Grundlegend hierfür ist die Verwendung hochspannungsbetriebener monolithischer aktiver Pixelsensoren (HV-MAPS) für den Spurdetektor. Diese enthalten schnelle Ausleseelektronik und können auf 50 µm gedünnt werden. Für die Pixelsensoren wird eine Leistungsaufnahme von $250\,\mathrm{mW/cm^2}$ erwartet. Um sie ausreichend zu kühlen ($0\,^\circ\mathrm{C} < T_{soll} < 70\,^\circ\mathrm{C}$) und gleichzeitig möglichst wenig zusätzliches Material in den Detektor einzubringen, soll er mit gasförmigem Helium gekühlt werden.
Im Rahmen dieser Arbeit wurde die Kühlung des Mu3e-Pixeldetektors mit gasförmigem Helium untersucht. Hierfür wurden zum einen Tests mit heizbaren Detektormodellen im Strömungskanal durchgeführt und zum anderen numerische Strömungsmechanik(CFD)-Simulationen. Die Ergebnisse beider Methoden sind konsistent und bestätigen, dass das geplante Kühlkonzept für das Mu3e-Experiment geeignet ist.

Contents

Chapter 1

Introduction

The Standard Model of particle physics is a very successful theory to describe the fundamental constituents of matter and their interactions. However, it still leaves some phenomena unexplained. For example, it does not include gravitation or any viable dark matter particle, and it does not explain baryogenesis. Furthermore, lepton flavor violation (LFV), which has been observed in the form of neutrino mixing, does not exist in the original SM. These limitations suggest that New Physics beyond the SM exists.
A variety of experimental searches for New Physics has been carried out, for example at the Large Hadron Collider (LHC) that operates at the high energy frontier and searches directly for new heavy particles. Another approach to New Physics searches makes use of the fact that, due to quantum effects, physics characterised by high mass scales also affects low energy processes. This enables New Physics searches at low energies, which require high precision in return.
The Mu3e experiment will search for the charged lepton flavor violating (CLFV) decay $\mu^+ \to e^+e^+e^-$. Since this decay is suppressed to unobservable levels in the SM, any signal would be a sign for New Physics beyond the SM. The goal is to reach a sensitivity for the branching ratio of 10^{-16} and, in case no signal is found, to set an upper limit for the branching ratio of 10^{-16} at 90 % CL, four orders of magnitude below the current limit.
The experimental concept is to stop a continuous high-intensity muon beam on an extended target and measure the decay electrons (positrons) with a tracking detector in a solenoidal magnetic field. Since the muons decay at rest, the energies of the decay electrons (positrons) are $\lesssim 53\,\mathrm{MeV}$. In this energy regime, multiple Coulomb scattering in the detector material is the dominating factor limiting the momentum and vertex resolution of the tracking detector. In order to reach the aimed sensitivity, high momentum, vertex and time resolution are required to suppress backgrounds. Therefore, the detector has to be optimized for a low material budget in the active area. The main part of the detector is a silicon pixel tracker consisting of four cylindrical layers of thin High-Voltage Monolithic Active Pixel Sensors (HV-MAPS). It is complemented by a time-of-flight system consisting of a scintillating fibre tracker and a scintillating tile detector.
The HV-MAPS chips include part of the readout electronics and are read out at high rates. Their power consumption is expected to be approximately $250\,\mathrm{mW/cm^2}$. Since also the cooling system must meet the requirement of a

low material budget, it is planned to cool the active detector parts with gaseous helium.
In the context of this thesis, the cooling concept for the Mu3e pixel detector has been investigated experimentally using heatable full-scale models of parts of the detector. Additionally, computational fluid dynamics (CFD) simulations were performed.
Chapter 2 gives a brief introduction to the Standard Model and lepton flavor violation. Chapter 3 provides an overview of the current situation in CLFV searches. A description of the experimental design of the Mu3e experiment is given in chapter 4. Chapter 5 constitutes the main part of this thesis. It includes discussions on experimental tests and CFD simulations of the gaseous helium cooling of the Mu3e pixel tracker. The part of section 5.4 on "Simulations with Local Cooling" is based on simulations carried out by Yanwing Ng [35]. Chapter 6 concludes this thesis with a summary and an outlook on possible future developments concerning the cooling of the Mu3e detector.

Chapter 2

Theoretical Background

2.1 The Standard Model of Particle Physics

The Standard Model of particle physics (SM) is a theory of the fundamental constituents of matter and their fundamental interactions, the electromagnetic interaction, the weak interaction and the strong interaction[1]. The building blocks of the SM are shown in figure 2.1.

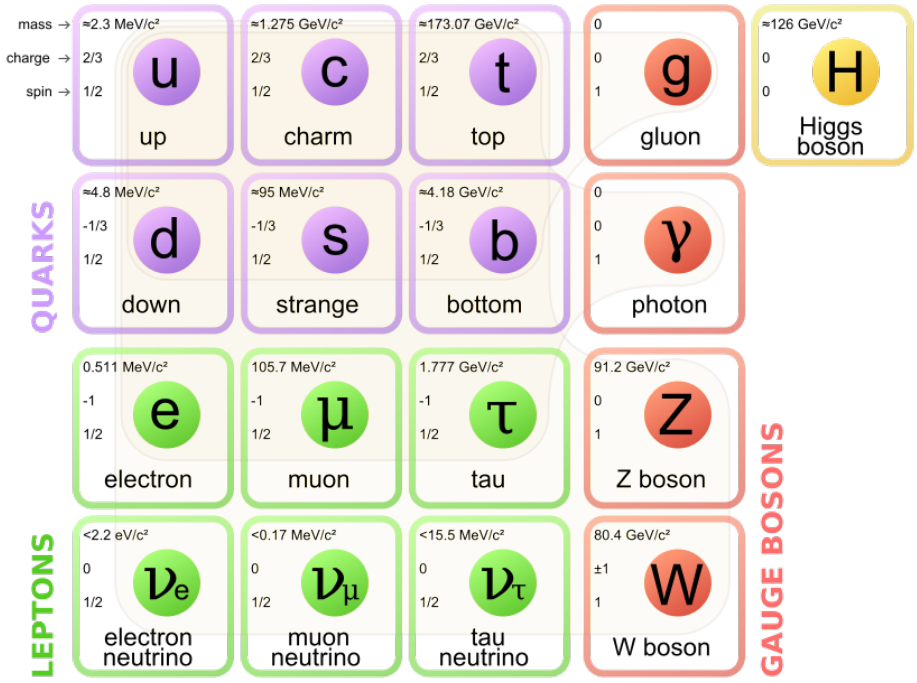

Figure 2.1: *Building blocks of the Standard Model [2]*

There are twelve spin-1/2 particles called fermions. Each of them has a corresponding antiparticle. They are classified according to which interactions they

[1]It does not include gravity.

can take part in.
Quarks are the only fermions that interact strongly. In nature, they do not appear as free particles, but only as strongly bound states called hadrons. Quarks also interact electromagnetically and weakly.
The remaining six fermions are called leptons. The electron, the muon and the tau carry electric charge -1. They interact electromagnetically and weakly. The three corresponding neutrinos carry no electric charge. They only interact weakly. In the original SM, neutrinos are massless.
The gauge bosons have spin 1. They are the mediators of the fundamental interactions. The gauge boson of the electromagnetic interaction is the photon. It couples to all particles that carry electric charge, and it is massless.
The weak interaction is mediated by the neutral Z boson and two electrically charged bosons $W^{\pm}$ with electric charges +1 and -1, respectively. The mass of the gauge boson affects the strength and range of the corresponding interaction. The fairly high masses of the Z and the W bosons (see figure 2.1) lead to a relatively small interaction strength and range. This is what gives the weak interaction its name.
The gauge boson of the strong interaction, the gluon, is massless and interacts with particles that have a property called color charge. Since, alongside quarks, gluons carry color charge themselves, they can interact with other gluons.
The SM particle that was observed last is the Higgs boson. In theory, it is part of the Higgs mechanism that generates the masses of all fundamental SM particles [3].
Although the SM provides a successful description of the fundamental particles and their interactions (excluding gravity) and can explain a large amount of experimental data, it still has limitations. For example, in the SM, neutrinos are massless, but experiments indicate that neutrinos do have masses. This problem is discussed in the following section 2.2.

2.2 Lepton Flavor Violation

The term flavor denotes the species of a particle. There are six quark flavors (up, down, strange, charm, top, bottom) and six lepton flavors (electron, muon, tau, electron neutrino, muon neutrino, tau neutrino). The flavor of quarks can change in weak interactions. This is due to the fact that the state of a freely propagating quark, i.e. the eigenstate of definite mass, does not equal the eigenstate of definite flavor, which is the state that takes part in weak interactions, but it is a superposition of flavor eigenstates. The information on the strength of flavor changing weak interactions is contained in the so-called Cabibbo-Kobayashi-Maskawa (CKM) matrix [4].
For leptons, no flavor changing interactions exist in the original SM. However, experimental results (from Super-Kamiokande [5], SNO [6], KamLAND [7], and others) indicate that neutrinos do change their flavor. A change of the lepton flavor in a physcial process is called lepton flavor violation (LFV).
The simplest way to extend the SM in such a way that it allows for LFV is to introduce the Pontecorvo-Maki-Nakagawa-Sakata (PMNS) matrix, the equivalent of the CKM matrix for leptons. This, however, requires neutrino mass differences, and therefore at least two neutrinos have to have masses, although they can still be very small.

While, today, neutrino mixing is considered a fact, there has never been any experimental evidence for leton flavor violation in the charged lepton sector (CLFV). Theoretically, charged lepton flavor violating processes can occur in the extension of the SM discussed above, but they are suppressed to unobservable levels due to the so-called GIM mechanism [8]. As an example, figure 2.2 shows the Feynman diagram of the process $\mu^+ \to e^+\gamma$. Its branching ratio is $BR(\mu^+ \to e^+\gamma) = \mathcal{O}(10^{-54})$ [11].

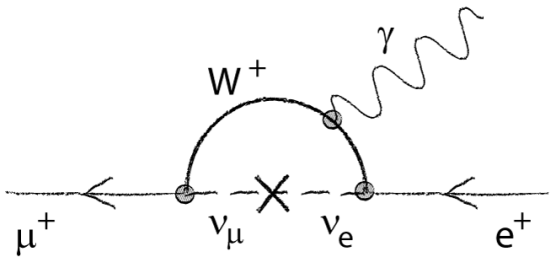

Figure 2.2: *Feynman diagram of the process $\mu^+ \to e^+\gamma$ in a minimal extension of the SM containing at least two massive neutrinos*

The Decay $\mu \to eee$ in New Physics Models

Because of the above, the observation of CLFV would be a clear sign for New Physics beyond the Standard Model. In contrast to the decay $\mu \to e\gamma$, where physics beyond the SM could only contribute via photon penguin diagrams (see figure 2.2), for the decay $\mu \to eee$ also Z penguin diagrams, tree-level diagrams and box diagrams could contribute [1].
There could for example be new supersymmetric (SUSY) particles running in the loop of a penguin diagram as shown in figure 2.3.

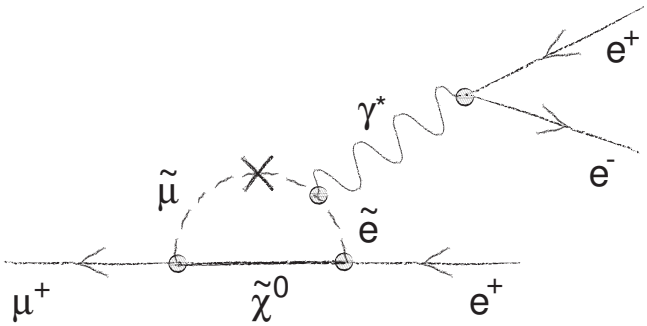

Figure 2.3: *Penguin diagram of the process $\mu^+ \to e^+e^+e^-$ with sparticles running in the loop*

There could also be tree-level diagrams involving new particles, denoted by X in figure 2.4. X could, for example, be a sneutrino in SUSY models with R-parity violation [12] or a new massive electrically neutral gauge boson Z' [13].

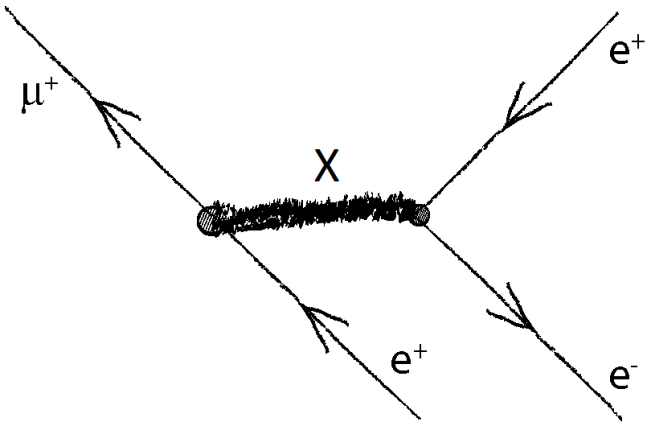

Figure 2.4: *Tree-level diagram of the decay $\mu^+ \to e^+e^+e^-$ proceeding by the exchange of a new particle X*

Chapter 3

Experimental Situation in CLFV Searches

There is a variety of experiments dedicated to the search of LFV in the charged lepton sector. Figure 3.1 gives an overview of the upper limits on the branching ratios of different CLFV processes, set by different experiments at 90 % CL over the last 70 years.
In the following, selected experiments dedicated to the search for specific CLFV processes are briefly discussed.

3.1 The SINDRUM Experiment

The SINDRUM experiment ran from 1983 to 1986 at the Paul Scherrer Institute (PSI) in Switzerland, searching for the decay $\mu^+ \to e^+e^+e^-$. Low energy muons were stopped on a hollow double cone target and the decay electrons were detected with multiwire proportional chambers and a trigger hodoscope placed in a 0.33 T solenoidal magnetic field. The estimated sensitivity for the process $\mu^+ \to e^+e^+e^-$ of approximately $5 \cdot 10^{-14}$ [16] was mainly limited by background from the process $\mu^+ \to e^+e^+e^-\nu_e\overline{\nu}_\mu$. No signal was found. The limit set for the branching ratio was $BR(\mu^+ \to e^+e^+e^-) < 1 \cdot 10^{-12}$ at 90 % CL [16]. It was basically determined by the limited number of stopped muons.

3.2 The MEG Experiment

The MEG experiment has been taking data since 2008, searching for the decay $\mu^+ \to e^+\gamma$. It is located at PSI. Low energy muons are stopped on a thin target. The decay positrons are detected in drift chambers and the photons in a liquid xenon calorimeter. The sensitivity is limited by accidental background. So far, no signal was found. The current limit on the branching ratio set by this experiment is $BR(\mu^+ \to e^+\gamma) < 5.7 \cdot 10^{-13}$ at 90 % CL [15].

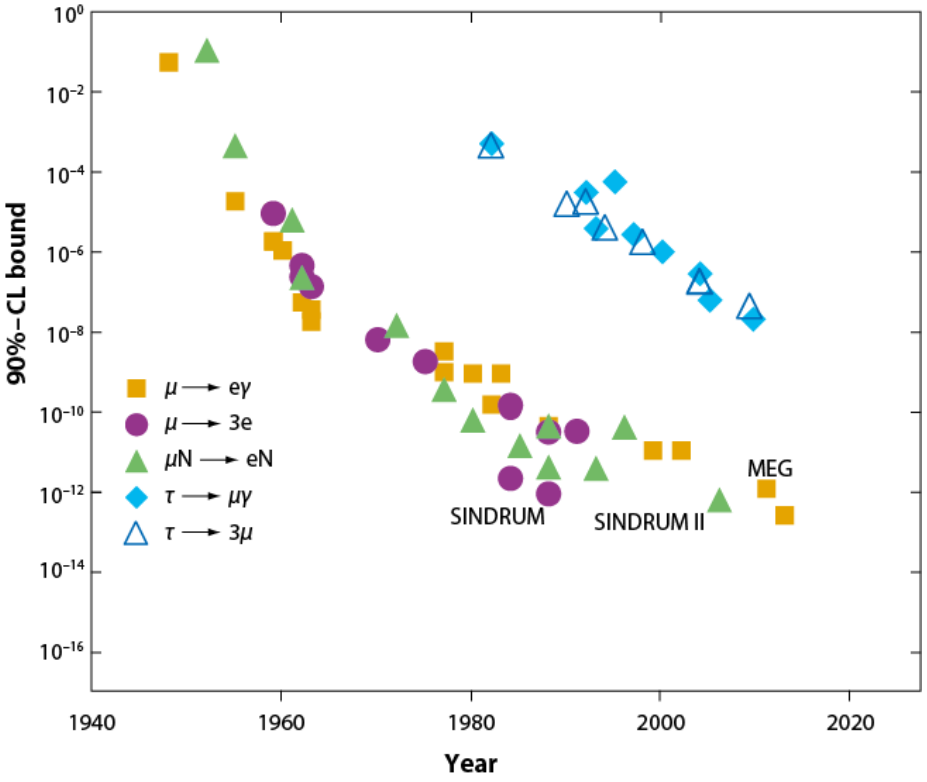

Figure 3.1: *Overview of the experimental results of various CLFV searches obtained over the last 70 years [14, 15]*

3.3 Other CLFV searches

Another CLFV process is $\mu^- \rightarrow e^-$ conversion. When a negative muon is stopped in matter, it forms a muonic atom and cascades down in energy levels to the ground state. Within the Standard Model, there are essentially two possibilities to what could happen next to the muon. Either it decays in orbit ($\mu^- \rightarrow e^- \nu_\mu \overline{\nu}_e$) or it is captured by the nucleus, producing a neutrino. In the context of New Physics, however, there is the additional possibility of having neutrinoless $\mu^- \rightarrow e^-$ conversion, resulting in a two body state with the signature of an electron of one specific energy [13]. Limits on this process have been obtained for various nuclei, for example by the SINDRUM II collaboration, where the strongest one is $BR(\mu^- + Au \rightarrow e^- + Au) < 7 \cdot 10^{-13}$ for a gold target [17]. New experiments are planned to search for this process with higher sensitivity (Mu2e [18], COMET and PRISM [19]).
A wide variety of τ decays has been studied at B-factories and limits down to approximately 10^{-8} have been obtained [20].
At the LHC, CLFV could be observed if, for example, new SUSY particles were discovered, or in Z boson decays [21].

Chapter 4

The Mu3e Experiment

The goal of the Mu3e experiment is to search for the charged lepton flavor violating decay $\mu^+ \to e^+e^+e^-$ with a sensitivity corresponding to the branching ratio limit of 10^{-16} at 90 % confidence level. This is four orders of magnitude below the current limit of $BR(\mu^+ \to e^+e^+e^-) < 1.0 \cdot 10^{-12}$ at 90 % CL set by the SINDRUM experiment [16].
The experiment will be performed at the Paul Scherrer Institute (PSI) in Switzerland. It will run in two phases. Phase I should validate the experimental concept and help gaining experience with the new technology while already aiming for a sensitivity for the branching ratio of 10^{-15}. This could be achieved by using only part of the instrumentation and readout system and with an already existing beamline. The latter delivers about $1 \cdot 10^8$ muons per second. Phase II will reach for the final sensitivity. This requires a new beamline, which provides at least $2 \cdot 10^9$ muons per second, for the experiment to run within a reasonable amount of data taking time [1].

4.1 The Decay $\mu^+ \to e^+e^+e^-$

In order to reach the aimed sensitivity for the branching ratio of 10^{-16} one must be able to discriminate between the signal decay $\mu^+ \to e^+e^+e^-$ and backgrounds mimicking the signal.

4.1.1 Kinematics

For the decay $\mu^+ \to e^+e^+e^-$, all decay particles originate simultaneously from a single common vertex. The invariant mass of the three decay particles equals the rest mass of the muon.

$$m_\mu^2 = \left(\sum_{i=1}^{3} p_i \right)^2 \tag{4.1}$$

with p_i being the four-momenta of the decay particles. Assuming that the muon decays at rest on a stopping target, the momenta $\vec{p_i}$ of the electrons (positrons) add up to zero:

$$\left| \sum_{i=1}^{3} \vec{p}_i \right| = 0\,. \tag{4.2}$$

All energies are smaller than half the muon mass, i.e. $E_i \lesssim 53\,\mathrm{MeV}$.

4.1.2 Background

There are essentially two background sources for the decay $\mu^+ \to e^+e^+e^-$. One is the radiative muon decay with internal conversion. The other is accidental background from wrongly reconstructed events.

Accidental Background

Accidental background originates from events where two positrons and an electron appear as if they were produced in a signal decay, although they actually originated from at least two independent processes.
One of the main processes contributing to accidental background is the ordinary Michel decay $\mu^+ \to e^+\nu\overline{\nu}$. Negatively charged electrons can for example come from Bhabha scattering of a positron from a Michel decay with an electron in the target material. Figure 4.1 shows schematically the signal decay and an accidental background event.

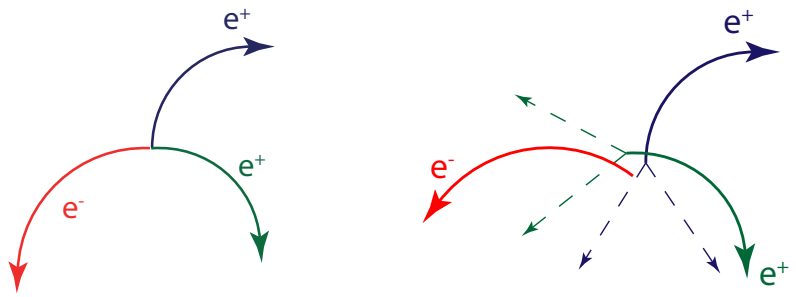

(a) *Signal event* ***(b)*** *Accidental background event*

Figure 4.1: *Schematic comparison of (a) the Mu3e signal event and (b) an accidental background event of two Michel decays with an additional electron*

Since the electrons (positrons) from accidental background events were not produced exactly simultaneously and at one single vertex, this kind of background can be suppressed by precise timing measurement and vertexing, in addition to precise momentum measurement.

Internal Conversion

The decay $\mu^+ \to e^+e^+e^-\nu_e\overline{\nu}_\mu$ is a radiative muon decay where the radiated photon immediately converts into an electron-positron pair. The corresponding Feynman diagram is shown in figure 4.2.
It can be distinguished from the signal decay only by the missing energy that is carried away by the two neutrinos. Therefore, this background can only be suppressed by reconstructing the neutrinos using energy and momentum

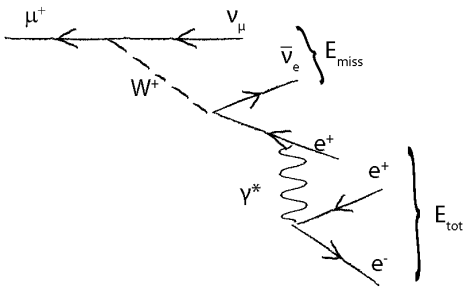

Figure 4.2: *Feynman diargam of the internal conversion decay* $\mu^+ \rightarrow e^+e^+e^-\nu_e\overline{\nu}_\mu$

conservation. Figure 4.3 shows the branching ratio of the internal conversion decay as a function of the missing energy cut. As one can see from this plot, a very high energy resolution is required.

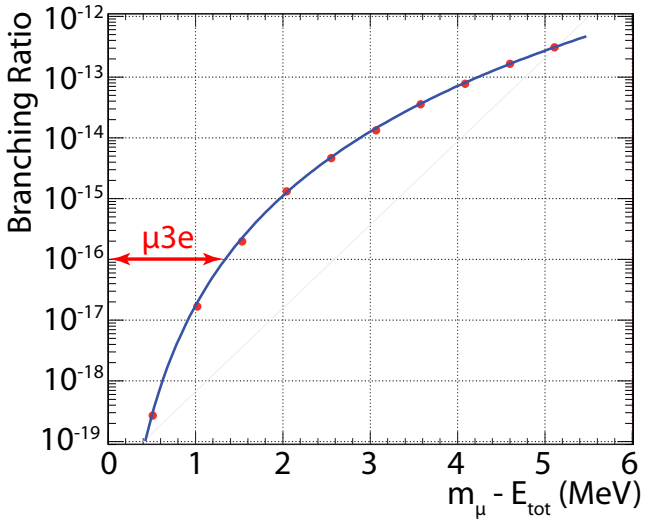

Figure 4.3: *Branching ratio of the internal conversion decay* $\mu^+ \rightarrow e^+e^+e^-\nu_e\overline{\nu}_\mu$ *as a function of the missing energy cut [9]*

4.2 The Mu3e Detector

4.2.1 Detector Concept

The muons will decay at rest after being stopped on a hollow double cone target made of thin aluminum (see figure 4.4).
As pointed out above, the Mu3e experiment requires high momentum resolution to suppress internal conversion background and good vertex and timing resolution to suppress accidental background. The decay electron (positron) momenta will be measured in a 1 T solenoidal magnetic field with a silicon pixel tracker

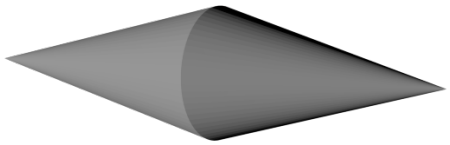

Figure 4.4: *Muon stopping target*

consisting of four cylindrical sensor layers. With electron energies smaller than 53 MeV, the dominating factor that limits the momentum and vertex resolution is multiple Coulomb scattering in the detector material. Therefore, it is crucial to keep the material budget in the active detector parts as small as possible. For better timing resolution, there will be additional timing detectors, a scintillating fibre hodoscope and a scintillating tile detector. Figures 4.5 and 4.6 show schematics of the detector, where the red (blue) lines are examples of positron (electron) tracks of a signal event.

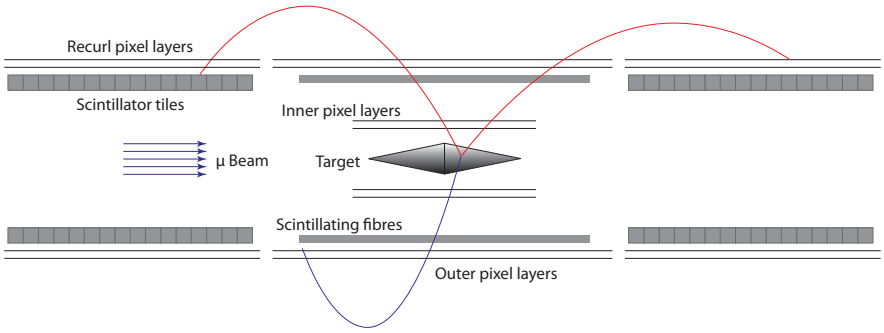

Figure 4.5: *Schematic of the detector cut along the beam axis*

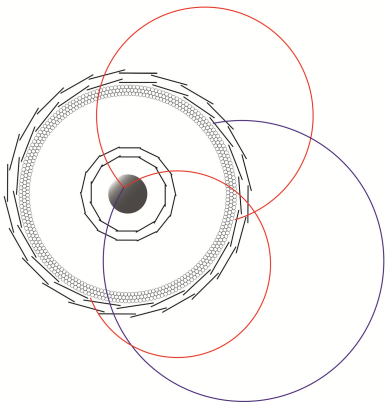

Figure 4.6: *Schematic of the detector cut transverse to the beam axis*

In the central detector region, there are four layers of silicon pixel sensors, an inner double layer around the target with radii of 2.4 cm and 3.0 cm and an outer double layer at radii of 7.3 cm and 8.5 cm. The outer double layer extends to both sides of the central detector to measure recurling electrons (positrons) to improve the precision of the momentum measurement. In figure 4.5, one can see one so-called recurl station on each side of the central detector. For the final phase II of the experiment, another one will be added on each side. The full detector will be approximately 2 m long.
In addition to the pixel tracker, there are two timing detectors placed underneath the outer two pixel tracker layers, a scintillating fibre tracker inside the central detector station and a scintillating tile detector inside the recurl stations.

Multiple Coulomb Scattering

Charged particles traversing a medium get deflected due to Coulomb interactions with nuclei. This effect is called multiple Coulomb scattering. It results in a displacement y and a deflection angle θ with respect to the undisturbed beam (see 4.7). The distribution of the scattering angles can be described by the theory of Molière. For small angles, it is approximately Gaussien and the following equation holds [22]:

$$\theta_0 = \frac{13.6\,\text{MeV}}{\beta cp} \cdot z \cdot \sqrt{\frac{x}{X_0}} \left(1 + 0.038\, log(\frac{x}{X_0})\right) \tag{4.3}$$

where θ_0 is the rms of the central 98 % of the planar scattering angle distribution, βc is the velocity of the incident particle, p its momentum, and z its charge number, x is the material thickness, and X_0 the radiation length. This means, the effect of multiple Coulomb scattering increases with material thickness, whereas it decreasas with increasing particle momenta.

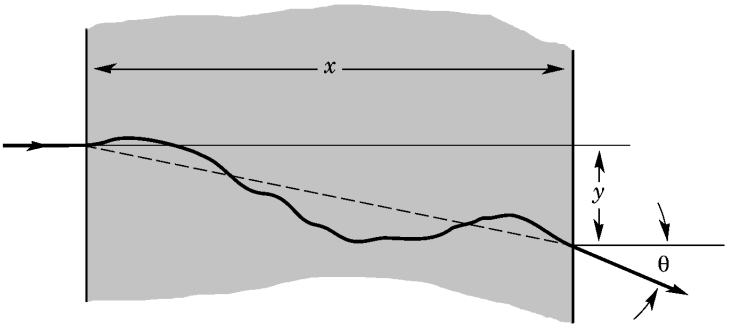

Figure 4.7: *Illustration of multiple Coulomb scattering, modified from [22]*

4.2.2 The Pixel Detector

Since the Mu3e experiment requires a minimal material budget in the active detector parts, while at the same time it has to cope with high muon decay rates, the silicon pixel tracker will consist of High-Voltage Monolithic Active Pixel Sensors (HV-MAPS) [10]. They can be read out fast and already include part of the read-out electronics, such that additional read-out chips are not

Component	Tickness [µm]	x/X_0 [%]
Support structure	25	0.018
Flex-print	25	0.018
Aluminum traces	12	0.013
HV-MAPS	50	0.053
Adhesive	10	0.003
Full layer	122	0.105

Table 4.1: *$\frac{x}{X_0}$ for the individual components of one pixel tracker layer*

required, and they can be thinned to 50 µm. It is planned that the signal and power lines consist of aluminum traces on flex-prints made of Kapton®[1] polyimide film, and that the support structure of the tracker modules consists of only 25 µm thin Kapton® foil. This design results in a thickness of $\frac{x}{X_0} \approx 0.1\,\%$ per tracker layer. The values for $\frac{x}{X_0}$ of the individual components of a tracker layer are summarized in table 4.1.

HV-MAPS

The pixel sensors used in the Mu3e experiment are silicon semiconductor detectors called High-Voltage Monolithic Active Pixel Sensors (HV-MAPS). They can be produced in a commercial high-voltage CMOS process. In the MAPS technology, the readout electronics is already integrated in the sensor. Therefore, no additional readout chip and no corresponding interconnecting bump bonds are needed. In contrast to ordinary MAPS designs, which collect ionization charges mainly via diffusion, HV-MAPS collect charges via drift due to the application of a high bias voltage in the order of $> 50\,\mathrm{V}$. This results in a time resolution of less than 10 ns as opposed to several hundred nanoseconds.
It is also important to note that CMOS circuits mainly dissipate power by charging and discharging various load capacities and therefore their power consumption depends on the data rate that they produce (dynamic power dissipation).
A schematic of a MAPS design is shown in 4.8.

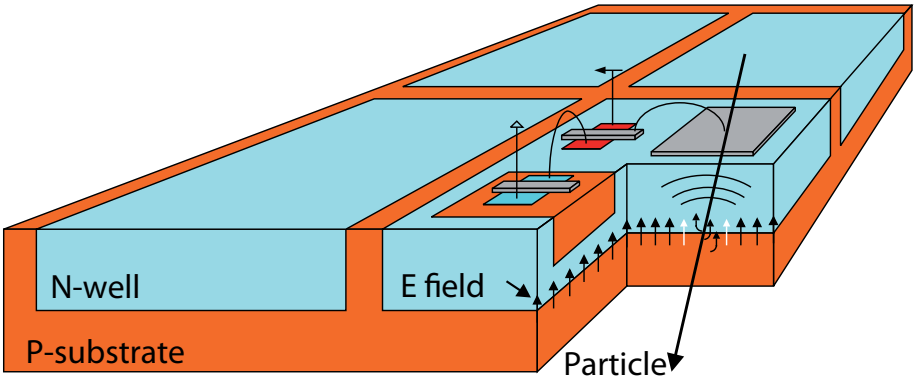

Figure 4.8: *Schematic of a MAPS design showing four pixels [10]*

[1] Kapton® is a registered trademark of E.I. du Pont de Nemours and Company.

The sensors for the Mu3e experiment are called MuPix. They will have a pixel size of $(80 \times 80)\,\mu m^2$, a sensor size of $(2 \times 2)\,cm^2$, and be thinned to $50\,\mu m$. Information on the MuPix power consumption and temperature characteristics can be found in section 5.2.

4.2.3 Mechanics

The mechanical design of the Mu3e detector has to be optimized mainly for a low material budget in the active detector region. Further requirements are mechanical stability and accessibility for assembly and repair.
The four cylindrical pixel tracker layers, labelled layer 1 to 4 from inside to outside, consist of the pixel sensors that are glued and bonded on flex-prints made of Kapton® polyimide film, which are in turn glued on a support structure made of 25 µm thin Kapton® film.
Since the sensors have an approximately 0.5 mm wide dead area because of the the digital readout part, there is an overlap between neighboring sensors of 1 mm (see figure 4.6).
The support structure is glued to plastic endpieces, which allow for the tracker modules to be mounted to endrings. A preliminary design of the endrings for the two outer tracker layers can be seen in figure 4.9.

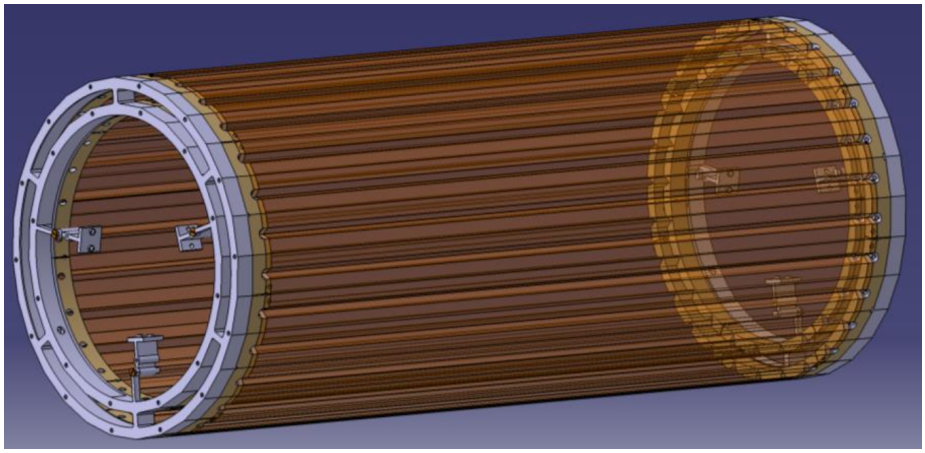

Figure 4.9: *Preliminary design of the pixel tracker endrings for layers 3 and 4*

This design includes a gas distribution system for cooling purposes.
One challenge, regarding the mechanical design, is distributing all sevices and the cooling gas to each detector station and providing accessibility for detector assembly, while at the same time minimizing the gaps between two stations for maximum detector acceptance.
For ease of production, assembly and repair, the detector layers are devided into several parts. The smaller inner two layers, which have an active length of 12 cm and are 8- and 10-sided, respectively, are each made of two halfs. Figure 4.10 shows a mechanical prototype of the inner two layers.
Layer 3 (24 sides) and layer 4 (28 sides) are made of modules that combine four sides and have an active length of 36 cm. In figure 4.11, a ptototype of a layer 3 module is shown.

Figure 4.10: *Prototype of the inner double layer of the pixel tracker*

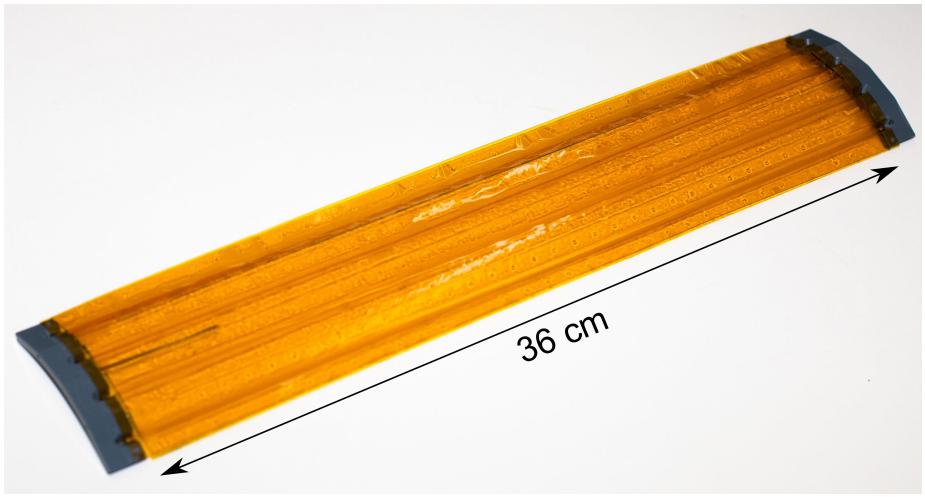

Figure 4.11: *Mechanical prototype of a layer 3 module*

For these prototypes, 50 µm thin glass was used to simulate the silicon sensors, because it has a comparable flexibility. The layer 3 and 4 modules feature a prism shaped fold in the Kapton support structure on each side (see figure 4.12). The folds increase the mechanical stability of a module significantly, while they add only little to its thickness, speaking in terms of fraction of radiation length. For the module production, special tools have been built that can be connected to vacuum pumps for holding the individual components of a module in place while the adhesive hardens. It is important that the adhesive is applied as a thin uniform layer. The tool for production of layer 2 is shown in figure 4.13.

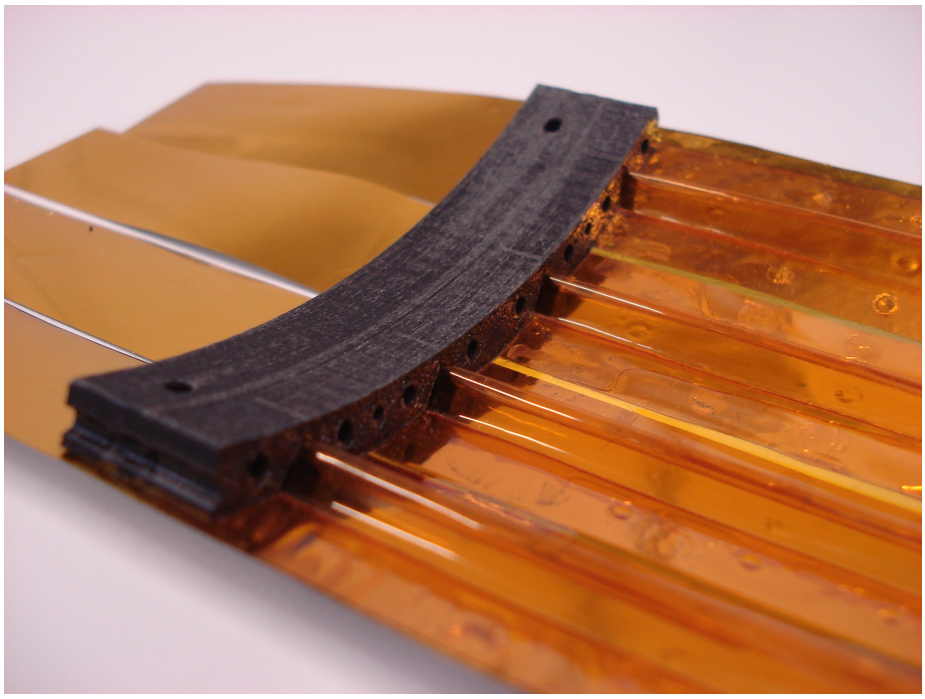

Figure 4.12: *Photo of a module prototype showing the prism shaped folds in the Kapton support structure*

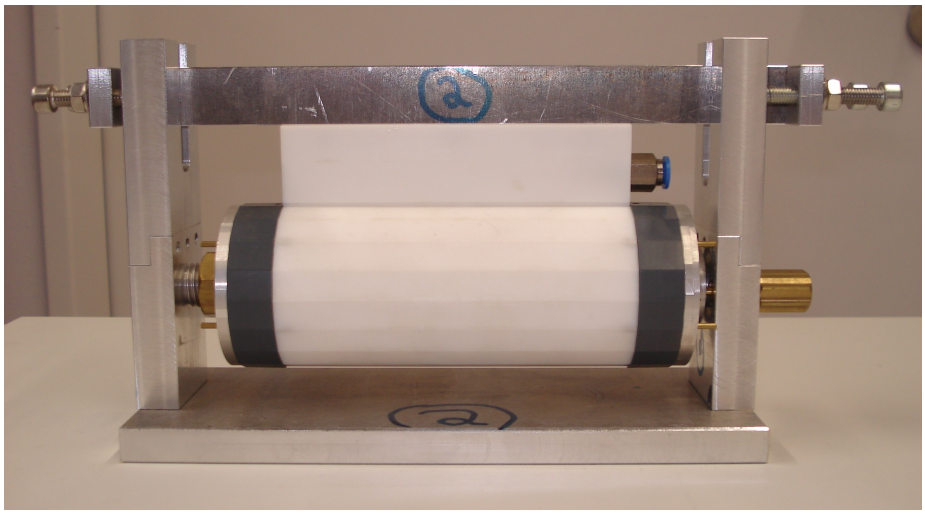

Figure 4.13: *Tool for the production of layer 2*

4.2.4 The Time of Flight Detector

In order to improve the time resolution of the Mu3e detector to suppress accidental background (see section 4.1.2), the pixel tracker is complemented by a time-of-flight system consisting of two parts. The first part is a scintillating fibre tracker with an expected time resolution $< 1\,\text{ns}$ that will be placed between the pixel layers of the central detector station. The second part is a scintillating tile detector that will be located inside the recurl stations. Its expected time resolution is below 100 ps.
Figure 4.14 displays the simulated events in one 50 ns readout frame at a muon stopping rate of $2 \cdot 10^9 \frac{1}{\text{s}}$. It shows the necessity of the timing information to prevent pileup. The timing information also allows for measuring the direction of propagation, i.e. the charge of the decay particles.

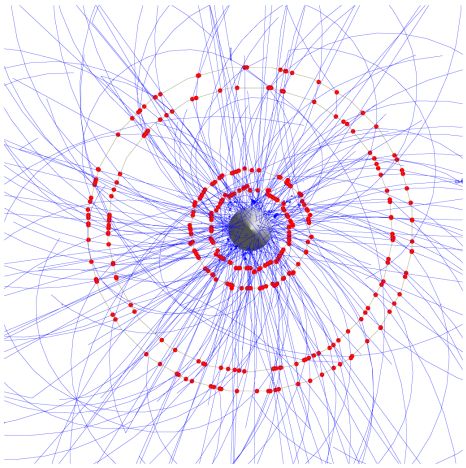

Figure 4.14: *Simulated event display of one* $50\,ns$ *readout frame at* $2 \cdot 10^9$ *muons per second*

The Fibre Detector

Since the fibre tracker is placed in the central detector, i.e. the active detector region, it aims for best possible time resolution ($< 1\,\text{ns}$) with minimum additional material. It is designed to consist of ribbons of two or three layers of scintillating fibres. The fibres are planned to have a diameter of 250 µm. The ribbons are 36 cm long and 1.6 cm wide, and the fibres are staggered as tightly as possible (see figure 4.15). The fibre tracker will be located between the pixel layers 2 and 3 at a radius of approximately 6 cm.
The photons produced in the fibres will be detected with silicon photomultipliers (SiPM) at both ends. SiPMs are very compact and can be operated at high counting rates, with high gain, and in high magnetic fields.

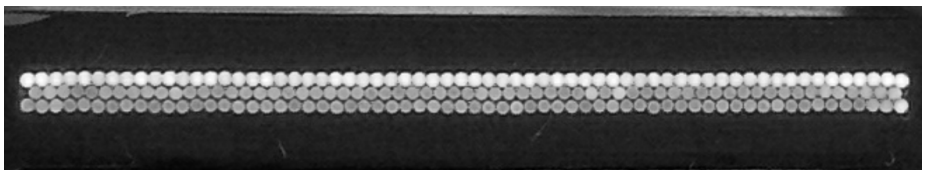

Figure 4.15: *Cross section of a fibre ribbon [23]*

The Tile Detector

The second part of the time-of flight-system, the scintillating tile detector, is located inside the recurl stations underneath the recurl pixel layers. Since it doesn't matter what happens to the recurling electrons (positrons) after they traverse the tile detector, the latter can be optimized solely for time resolution. The detector consists of plastic scintillating tiles with a size of about $0.5\,\mathrm{cm}^3$. They are read out by SiPMs and a custom ASIC called STiC [24]. A time resolution of 100 ps is aimed for.

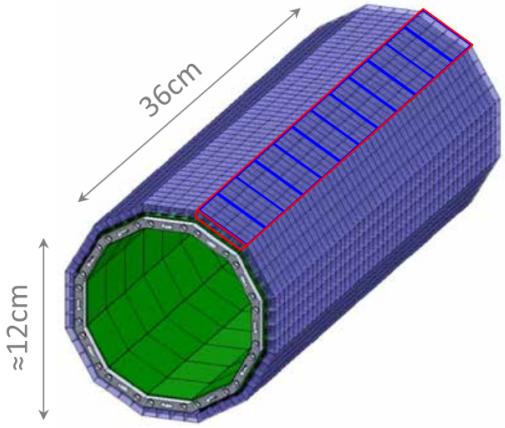

Figure 4.16: *Drawing of the tile detector for one recurl station including readout electronics (green)*

4.2.5 Data Acquisition

The Mu3e readout scheme is shown in figure 4.17. The system works without a hardware trigger, i.e. the detector elements continuously send zero-suppressed hit information to the data acquisition (DAQ) system. The data rate is of the order of 1 Tbit/s. The data is first sent to front-end FPGAs (field-programmable gate arrays), which are located inside the recurl stations. Via readout boards, one selected time slice of the complete detector information is sent to one filter farm PC at a time. Here, events are reconstructed online. Selected events are sent to a single data collection server at a rate of the order of 50 Mbytes/s and are then written to a mass storage system.

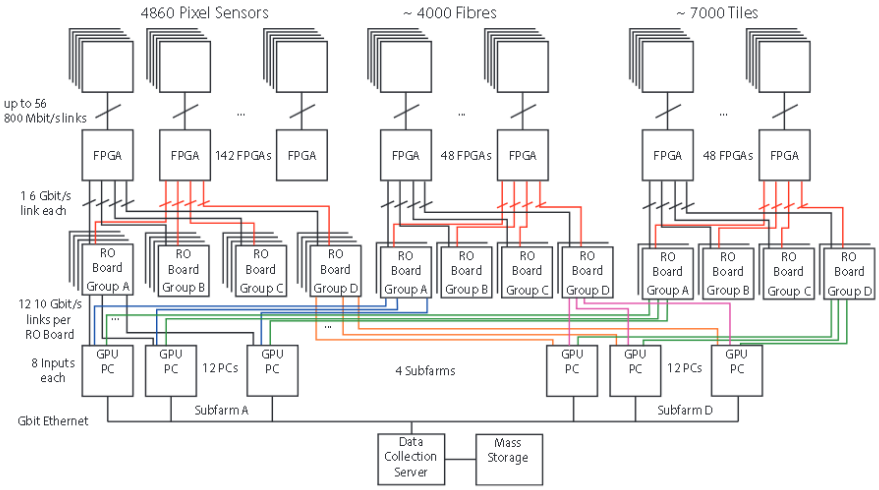

Figure 4.17: *Mu3e readout scheme*

Chapter 5

Cooling of the Mu3e Pixel Detector

It is one challenge of the Mu3e experiment to build a detector with a very low material budget to minimize multiple scattering of the decay electrons (positrons). To add as little material as possible to the detector for the cooling system, the basic idea is to cool the pixel detector with a global flow of gaseous helium that runs through the complete detector volume. Helium was chosen as coolant because of its radiation length. For a helium layer of 1 m, the thickness in units of the radiation length $\frac{x}{X_0}$ is approximately 0.019 %. In contrast, $\frac{x}{X_0} \approx 0.3\,\%$ for 1 m of nitrogen, and $\frac{x}{X_0} \approx 0.1\,\%$ for one tracker layer. In addition to that, helium has good cooling capabilities based on its molecular properties (see section 5.1).
The cooling system must be capable of keeping the temperature of the pixel detector below 70 °C (upper edge of the pixel sensors' operating range). The target value for the heat dissipation per surface area P/A of the pixel tracker is $150\,\mathrm{mW/cm^2}$. Tests with sensor prototypes showed that a value of $250\,\mathrm{mW/cm^2}$ is more realistic (see section 5.2). Assuming a power consumption per surface area of $250\,\mathrm{mW/cm^2}$, the full Mu3e pixel tracker has a total power consumption of the order of 5 kW.
It is planned to have an additional liquid cooling system for the readout electronics inside the inactive parts of the detector, which is not discussed further in this thesis.
A successful example of a similar cooling system is that of the STAR Silicon Vertex Tracker, where an open air flow removes about 180 W of heat from the detector volume [25].
In the proposed cooling system for the Mu3e pixel detector, the helium runs through a closed loop including the Mu3e detector and a heat exchanger pipe. The latter cools the warm helium coming from the detector down to the favoured temperature at which it is to re-enter the detector. This temperature should be set slightly above 0 °C to prevent potential water entering the detector from freezing. The heat exchanger tube is connected via a separate cooling curcuit to a cooling unit, which has already been acquired. It has a specified maximum cooling power of 20 kW.
To increase the overall cooling capability and to achieve a more unifrom tem-

perature distribution throughout the detector volume, a system for local helium distribution is planned, which complements the global helium flow that runs openly through the complete interior of the magnet. This system allows for distributing helium directly to each pixel layer of each of the five detector stations (see section 5.3.7).
To investigate the cooling concept for the Mu3e pixel detector, tests with heatable detector models as well as computational fluid dynamics (CFD) simulations have been carried out. This thesis follows up two prior theses on the same topic [26, 27].
The first section of this chapter (section 5.1) gives an overview of the theory of convective heat transfer. In the following section 5.2, information on the MuPix power consumption and temperature characteristics is provided. In section 5.3, the procedure and the results of experimental cooling tests are presented for the global and the local cooling system. The according CFD simulations are discussed in section 5.4. The last section of this chapter, section 5.5, addresses the issue of flow induced vibrations and presents a method to measure them.

5.1 Cooling of a Heated Surface by Forced Convection

The cooling of a heated surface by a fluid (gas or liquid) flowing over it is discribed by the heat transfer process called convection. In principle, a heated surface also dissipates energy in the form of thermal radiation. For the temperature regime under consideration, it is, however, assumed that this effect is negligibly small compared to the heat dissipation by convection [26].
Convection is a combination of two mechanisms, energy transfer by diffusion (random molecular motion) and the macroscopic motion of the fluid. The latter form of energy transfer is called advection and has to be described by fluid mechanics.
If the fluid flow is caused by external means, such as a fan or a pump, one speaks of forced convection. In contrast, natural convection is caused by density differences due to temperature variations in the fluid.
For understanding convective heat transfer of a fluid flowing over a heated surface, the concept of boundary layers is crucial. Two kinds of boundary layers have to be considered. The velocity boundary layer is the region in which the velocity varies from $v = 0\,\frac{m}{s}$ at the surface to a finite velocity v_∞ associated with the flow. Its thickness δ is typically defined as the distance from the surface where $v = 0.99 \cdot v_\infty$. Analogously, the thermal boundary layer is the region where the temperature varies from T_s, the surface temerature, to the temperature T_∞ of the outer flow. Its thickness δ_T is defined as the distance from the surface where $T_s - T = 0.99(T_s - T_\infty)$. Figure 5.1 illustrates both the thermal and the velocity boundary layer over a flat plate.
When dealing with a convection problem, it is important to determine whether the flow in the boundary layer is laminar or turbulent. In a laminar boundary layer, fluid flow is highly ordered and one can identify streamlines along which fluid particles move. In contrast, the flow in a turbulent boundary layer is irregular and characterised by random motions of fluid particles. A transition from laminar to turbulent flow occurs, when small perturbations in the flow

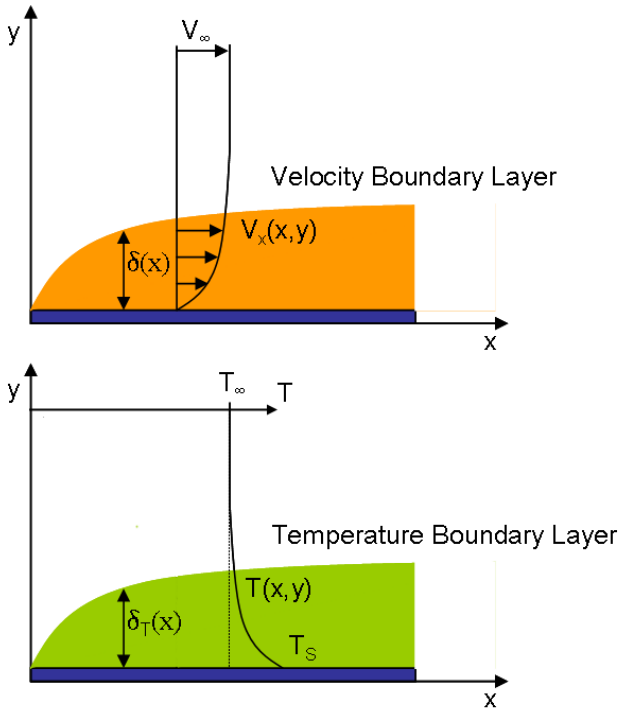

Figure 5.1: *Illustration of the thermal and velocity boundary layers, modified from [34]*

cannot be damped away by viscous forces. An indicator for which of the two flow regimes one is dealing with is the dimensionless Reynolds number

$$Re = \frac{vL}{\nu} \tag{5.1}$$

where v is the mean flow velocity, L is a characteristic length and ν is the kinematic viscosity. It represents the ratio of inertia to viscous forces. For example, for a flat plate, L is the distance from the leading edge. The critical Reynolds number Re_c, i.e. the value of the Reynolds number where the transition from laminar to turbulent flow occurs, is highly dependent on, for example, the surface roughness. For the flow over a flat plate, Re_c is known to vary from approximately 10^5 to $3 \cdot 10^6$ [31].
In the following, the theory of convective heat transfer is presented using the example of a two-dimensional, incompressible, laminar flow over a flat surface. More detailed calculations can be found in [26].

Laminar Flow over a Flat Surface

If one wants to calculate the heat flux from a heated surface to a fluid flowing over it, the first step is to determine the velocity field by solving the Navier-Stokes equations, the equations of motion of a fluid. For incompressible flow ($\nabla \vec{v} = 0$), they can be written in the form

$$\rho\left(\frac{\partial\vec{v}}{\partial t}+(\vec{v}\cdot\nabla)\vec{v}\right)=-\nabla p+\mu\Delta\vec{v}+\vec{f} \tag{5.2}$$

where ρ is the fluid density, p is the pressure, μ is the dynamic viscosity and $\vec{f}$ is the body force density. For the problem under consideration, they simplify to

$$v_x\frac{\partial v_x}{\partial x}+v_y\frac{\partial v_x}{\partial y}=\nu\frac{\partial^2 v_x}{\partial y^2} \tag{5.3}$$

The boundary conditions are

$$v_x(y=0)=v_y(y=0)=0 \tag{5.4}$$
$$v_x(y=\infty)=v_\infty \tag{5.5}$$

By solving (5.3) numerically, one obtains the velocity profile $v_x(y)$, which is indicated in figure 5.1.
The next step is to derive a temperature profile using $v_x(y)$ and the energy equation for a constant pressure flow field:

$$\rho c_p\left(\frac{\partial T}{\partial t}+\vec{v}\cdot\nabla T\right)=k\Delta T+\frac{d\rho_q}{dt} \tag{5.6}$$

where c_p is the specific heat capacity at constant pressure, k is the thermal conductivity, and ρ_q is the heat density. The equation one has to solve looks similar to (5.3):

$$v_x\frac{\partial T}{\partial x}+v_y\frac{\partial T}{\partial y}=\alpha\frac{\partial^2 T}{\partial y^2} \tag{5.7}$$

where $\alpha=\frac{k}{\rho c_p}$ is the thermal diffusivity. Solving (5.7) with the boundary condition of a constant heat flux $q=-k\frac{\partial T}{\partial y}\big|_{y=0}$ from the surface to the fluid, which is only an approximation, gives

$$Nu_x=0.453\cdot Re_x^{1/2}Pr^{1/3}\qquad Pr\geq 0.6 \tag{5.8}$$

with the dimensionless Nusselt number $Nu_x=\frac{hx}{k}$, which gives the ratio of convective heat transfer to conductive heat transfer. $h=\frac{q}{\Delta T}$ is the convective heat transfer coefficient, where in this case $\Delta T=T_s-T_\infty$.
$Pr=\frac{\nu}{\alpha}$ is the Prandtl number. It can be looked up to be 0.664 for helium [32]. Inserting the definitions of Nu_x and Re_x into (5.8) yields

$$\Delta T(x)=\frac{q}{0.453\cdot k\cdot Pr^{1/3}}\sqrt{\frac{\nu x}{v_\infty}} \tag{5.9}$$

for the temperature profile on the surface. With a surface of finite length L, one obtains

$$\Delta T_{max}=\frac{q}{0.453\cdot k\cdot Pr^{1/3}}\sqrt{\frac{\nu L}{v_\infty}} \tag{5.10}$$

Apart from an offset, the relation $\Delta T_{max}\propto\frac{1}{\sqrt{v_\infty}}$ could be varified experimentally for a cylinder barrel cooled on both the inside and the outside (see section 5.3.5). From (5.10), it becomes clear that the cooling capability of helium should be much higher than that of air since $\frac{k_{he}}{k_{air}}\approx 6$.

Tube with Triangular Cross Section

A more involved problem is the analysis of convective heat transfer of the flow inside a tube with triangular cross section. It is addressed here, because this situation is realised for the local cooling system presented in section 5.3.7.
For noncircular tubes, in some cases, results of circular tubes can be applied by using the hydraulic diameter

$$D_h = \frac{4A_c}{P} \tag{5.11}$$

where A_c is the cross-section area of the pipe and P is the wetted perimeter. For an isosceles triangle, it is $D_h = \frac{b}{a}\sqrt{a^2 + (\frac{b}{2})^2}$, where a denotes the two sides of equal length and b the third side. With this, one can for example calculate the Reynolds number. For a circular tube, it is in general given by

$$Re = \frac{vD}{\nu} \tag{5.12}$$

with the diameter D. Inserting the values $a = 4.6\,\mathrm{mm}$, $b = 5\,\mathrm{mm}$, $v = 20\,\frac{\mathrm{m}}{\mathrm{s}}$, and $\nu = 1.173 \cdot 10^{-4}\,\frac{\mathrm{m}^2}{\mathrm{s}}$ (helium) yields $Re \approx 730$. Turbulences are expected to occur at $Re_c \gtrsim 2300$ [31]. So, for the specified values, it is reasonable to assume laminar flow.
For laminar flow in a circular tube, the Nusselt number can be calculated theoretically, again with the approximation of a constant heat flow q at the tube walls, to be a constant $Nu = 4.36$ [31]. However, in the case of liminar flow, as opposed to turbulent flow, it is not so accurate to use circular tube results for the Nusselt number, especially with cross sections characterized by sharp corners [31]. More accurate results can be obtained by the use of differential energy and momentum equations [31], which shall not be discussed further in the context of this thesis.

5.2 MuPix Temperature Characteristics and Power Consumption

The Mu3e silicon pixel detector will consist of HV-MAPS (see section 4.2.2). The chips designed for the Mu3e experiment are called MuPix. The final chip is planned to have a size of $(2 \times 2)\,\mathrm{cm}^2$ and a pixel size of $(80 \times 80)\,\mu\mathrm{m}^2$. It will be thinned to $50\,\mu\mathrm{m}$. The power consumption and temperature characteristics of the MuPix determine the cooling capabilities that are required for the Mu3e experiment. Accordingly, studies have been performed with several different MuPix prototypes [28, 29].
The target value for the MuPix power consumption is $P/A = 150\,\mathrm{mW/cm}^2$. An upper limit for the operating temperature was set to $70\,^\circ\mathrm{C}$.
For the fifth generation of MuPix chips, called MuPix6, power consumptions between $223\,\mathrm{mW/cm}^2$ and $1\,\mathrm{W/cm}^2$ were measured. The lower value was obtained with DAC (digital-to-analog converter) settings that were optimized for low power consumption, while still resulting in an acceptable performance (signal-to-noise ratio of 10.5 ± 0.7) [28]. Concerning temperature characteristics, studies were performed for MuPix4, the fourth generation of MuPix, and Mupix6, where the influence of the operating temperature on the signal shaping was investigated. This was done by determining the peak position of the time-over-threshold (ToT) spectrum of the signal produced by $5.9\,\mathrm{keV}$ γ-rays of an $^{55}\mathrm{Fe}$ source at different temperatures. Therefore the setup was placed in a climate chamber. Figure 5.2 shows a MuPix6 chip on its readout PCB placed in the climate chamber. The temperature was monitored with a Pt100 thermometer. The results are shown in figure 5.3.

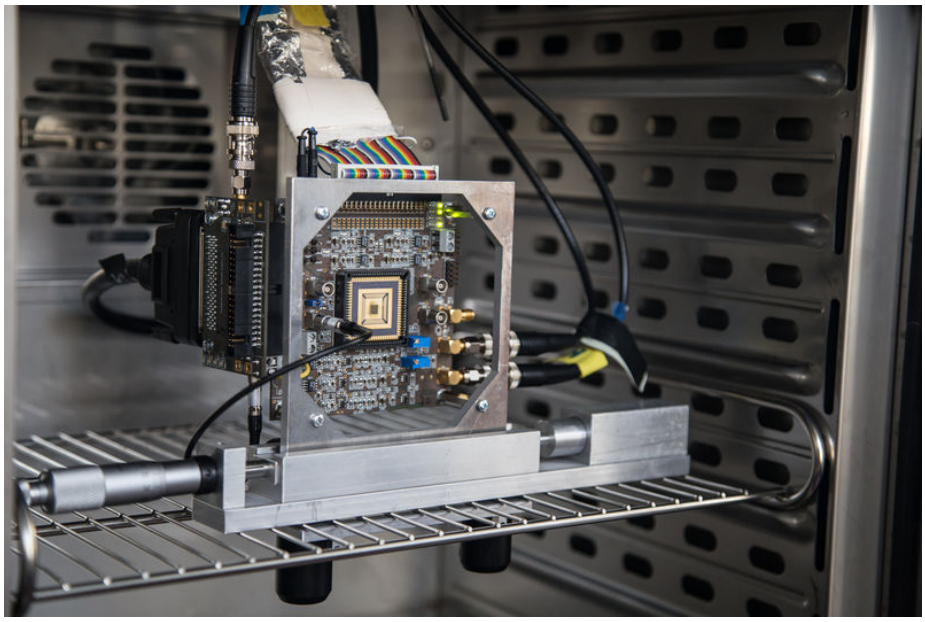

Figure 5.2: *Setup to measure the temperature dependence of the MuPix signal shaping including a MuPix6 chip on a readout PCB placed in a climate chamber*

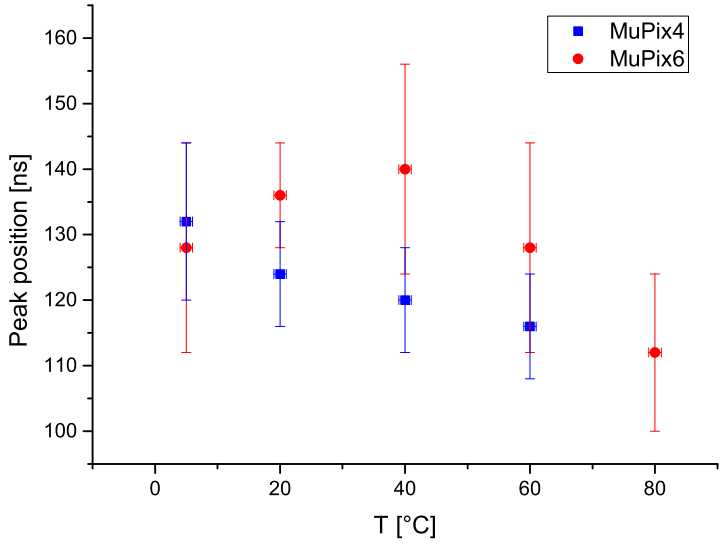

Figure 5.3: *Peak position of the ToT spectrum of* $5.9\,keV$ ^{55}Fe γ*-rays plotted against the temperature*

One can observe a slight tendency of the peak position to decrease with increasing temperature, but the size of the effect is only of the order of the error bars. For MuPix4, also the signal-to-noise ratio (SNR) was measured at different temperatures. At 24 °C, a SNR of 37.0 was obtained. At 70 °C, it was 31.5, which is still an adequate result [29].
In conclusion, one can assume that the MuPix sensors can be operated at temperatures between 0 °C and 70 °C and that temperature differences in the detector do not affect the momentum measurement as long as they are within that range. Furthermore, a power consumption of approximately $250\,mW/cm^2$ should be expected. To be on the safe side, the investigation of the cooling concept for the Mu3e pixel detector was performed with heating powers up to $400\,mW/cm^2$.

5.3 Cooling Tests with Heatable Detector Models

To test the cooling concept for the Mu3e pixel detector, two different heatable detector models were built. The first one is a full-scale model of layer 3 and layer 4 of one detector station with simplified geometry. The second one represents only a cutout of layer 3 and layer 4, but its geometry is similar to that of the real detector. Both models consist of a laminate of aluminum and Kapton® film. Therefore, they can be heated ohmically. They are equipped with Pt1000 temperature sensors. For cooling tests, they are placed inside an approximately 1 m long acrylic glass tube with a diameter of 22 cm, which acts as a flow channel. A gas flow is created by fans flanged on both ends of the tube. A more detailed description of both models and the experimental setup is given below.

5.3.1 Experimental Setup

Inside the flow channel, a uniform gas flow is produced in the direction parallel to the beam axis. The fans are connected to a power supply that can provide a maximum voltage of 23 V. The detector model is held in place by aluminum end rings. To heat the detector model ohmically, it is connected to several power supplies. The power cables are lead through holes in the flow channel. A vane anemometer is placed in front of the flow channel (see figure 5.7) to measure the gas flow velocity (on the input side). The anemometer has an integrated thermometer, which allows for measuring the temperature of the incoming cooling gas.
Pt1000 temperature sensors were glued directly ontop of both layers of each detector model in line with the beam axis (see figure 5.11). This allows for measuring temperature profiles on the models.
For the first tests, the setup was placed openly in the lab (see figure 5.4). Consequently, ambient air was used as coolant. Later, the setup was modified for cooling tests with helium (see section 5.3.6).

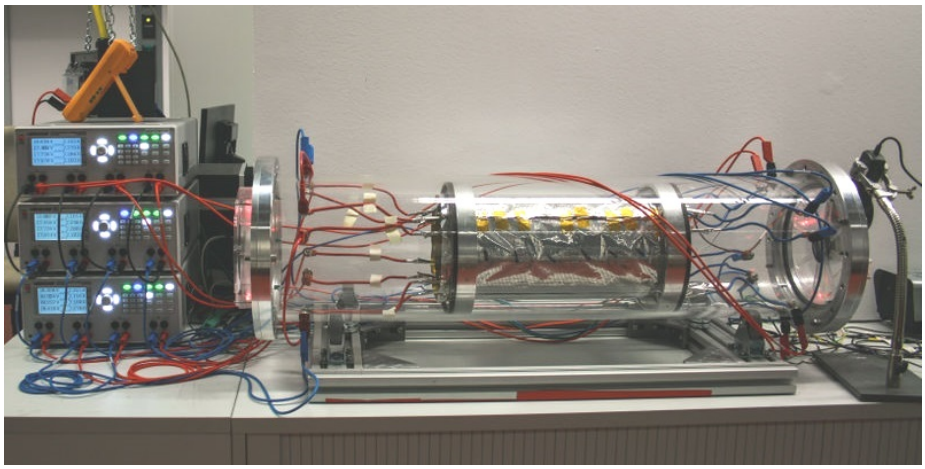

Figure 5.4: *Experimental setup for cooling tests with air during operation*

5.3.2 Temperature Sensor Readout

The Pt1000 resistance thermometers that the detector models are equipped with are each supplied with a constant current of 1 mA by a custom-built stable current source with a total of ten outputs [26]. Differential voltage signals from each output are transmitted via a flat ribbon cable to different channels of an ADC (analog-to-digital converter) in a LogicBox DL706[1]. The latter is connected via USB to a PC, where the data is read out and processed further using LabVIEW™[2] software [30, 26, 27]. Figure 5.5 shows the corresponding user interface. N sets the number of data points to be taken by each temperature sensor in one run, where each data point is the average of ten single measurements. The heating power, the temperature of the incoming cooling gas, the voltage supplied to the fans and the flow velocity must be typed in manually. The plots called "Kanal 0" to "Kanal 7" show the time evolution of the temperatures measured by the individual sensors. The additional plot at the bottom left shows the latest values of all sensors plotted against the sensor position. All data of one run is written to a file for offline analysis. An excerpt from the according program code can be found in Appendix B.

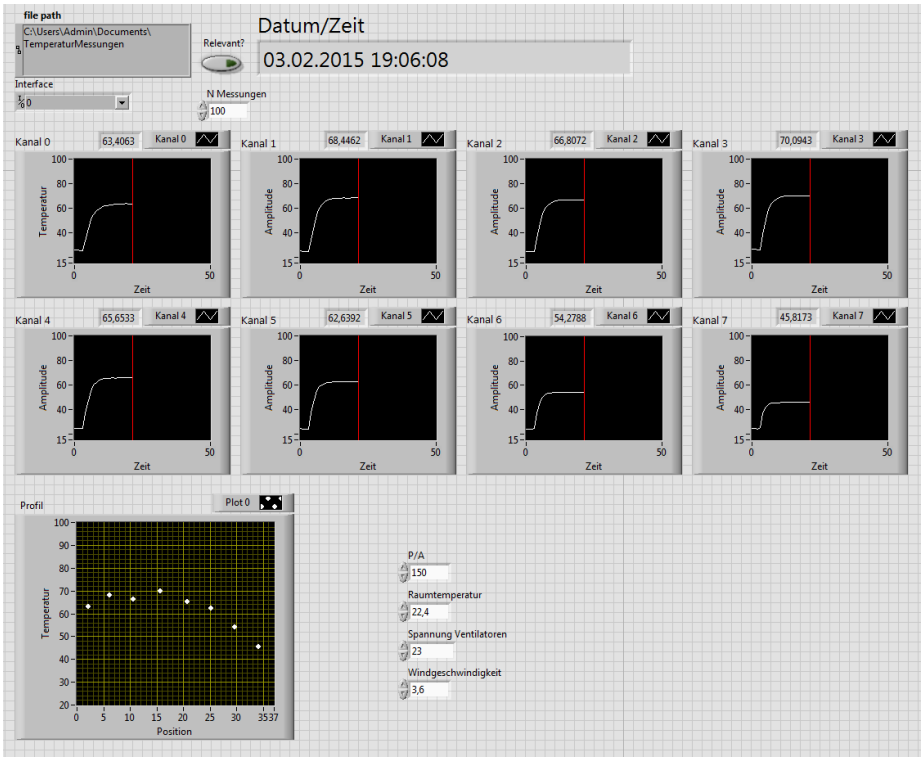

Figure 5.5: *User interface of the temperature readout software*

[1] universal DAQ-system produced in the electronics workshop of the Institute of Physics in Heidelberg

[2] LabVIEW™ is a trademark of National Instruments.

5.3.3 Temperature Sensor Calibration

For the cooling tests, temperatures between 20 °C and 100 °C were explored. Within that range, the resistance-temperature relationship of the Pt1000 sensors is in good approximation linear:

$$R(T) = R_0 + aT \tag{5.13}$$

with constants a and R_0.
The sensors were calibrated in an oven. The reference temperatures were monitored with a Pt100 thermometer and were varied between 20 °C and 100 °C in steps of roughly 10 °C. A staight line was fit to the data, according to (5.13), with fit parameters a and R_0. The results were entered into the readout program to convert the measured resistance into a temperature. Fig. 5.6 shows an example of a straight line fit to the calibration data of one sensor.

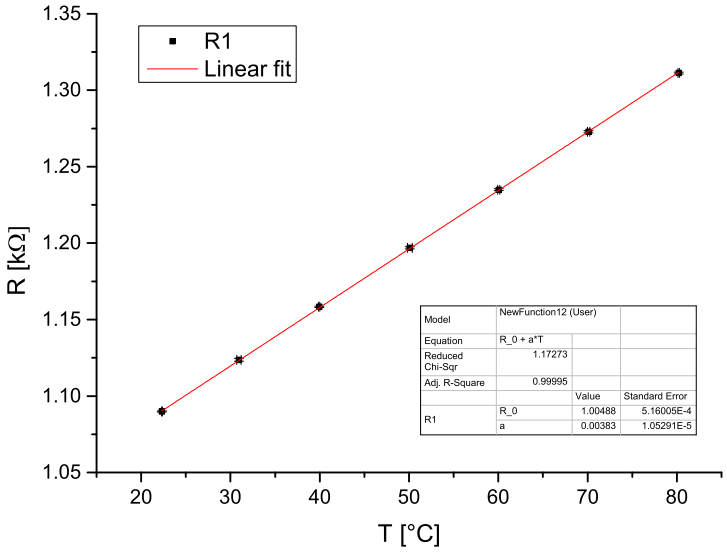

Figure 5.6: *Exemplary straight line fit to the calibration data of one Pt1000 sensor*

From the calibration of the sensor with the largest relative errors of the fit parameters ($\frac{\Delta R_0}{R_0} \approx 7.4{\cdot}10^{-4}$, $\frac{\Delta a}{a} \approx 3.4{\cdot}10^{-3}$), a calibration error was estimated:

$$\Delta T_{cal} = \sqrt{(\frac{\Delta R_0}{a})^2 + (\frac{R_0}{a^2}\Delta a)^2} \approx 0.9\,^\circ\mathrm{C} \tag{5.14}$$

This error was rounded up to $\Delta T_{cal} = 1\,^\circ\mathrm{C}$ and was used for all temperature sensors.

5.3.4 Flow Velocity Measurement

To quantize the flow of the cooling gas, the flow velocity is measured with a vane anemometer that is placed directly in front of the flow channel (on the input side) (see figure 5.7).

(a) During operation *(b) Display*

Figure 5.7: *Vane anemometer used for flow velocity measurements [27]*

The data has to be entered into the readout program manually. Since the measurement is sensitive to the position and the angle of the anemometer, the latter was positioned such that the maximum flow velocity was measured to ensure reproducibility. The measured velocities for a specific fan voltage setting fluctuate significantly. Figure 5.8 shows the flow velocities read off the anemometer display over the time interval of approximately 14 minutes, which corresponds to the duration of a temperature measurement run with 100 data points per sensor.
The average flow velocity and the standard deviation of this measurement are $(3.51 \pm 0.07)\,\frac{\mathrm{m}}{\mathrm{s}}$. Since the standard deviation is smaller than the smallest increment of the flow velocity measurement, the error of the measured flow velocity is set equal to the latter, i.e. $\Delta v = 0.1\,\frac{\mathrm{m}}{\mathrm{s}}$.

Flow Velocity Measurement in Helium

Measuring the flow velocity in helium poses a problem because the used anemometer is only calibrated for air. In general, commercial products for measuring helium flow velocities via an immersion sensor are very expensive. To estimate the helium flow velocity at least roughly, an attempt was made to recalibrate the vane anemometer for helium. This was done by connecting the anemometer via a diffusor to the pressure regulator of a helium bottle. The helium flow was

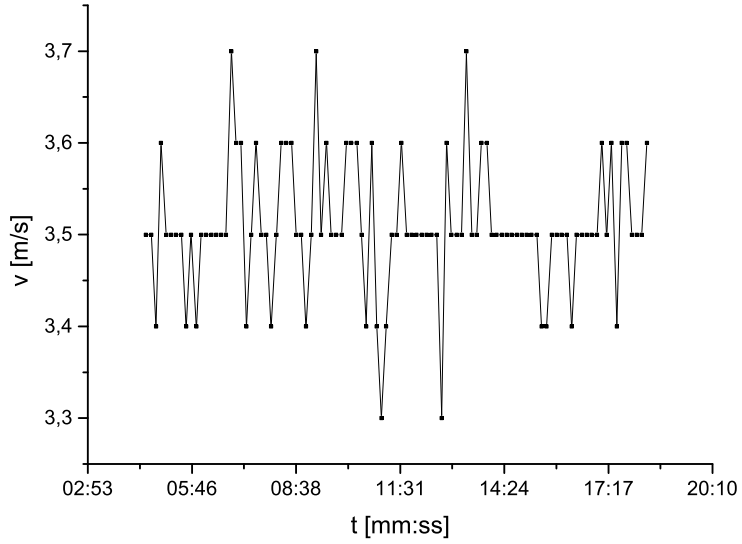

Figure 5.8: *Flow velocity of air measured with a vane anemometer and read off over the time interval of about 14 minutes*

estimated by measuring the time t in which the pressure of the helium bottle decreased by a certain amount Δp. With the ideal gas equation

$$pV = nRT \tag{5.15}$$

one can calculate the amount of substance streaming out of the bottle:

$$\Delta n = \frac{\Delta p V_{bottle}}{RT} \tag{5.16}$$

where V_{bottle} is the volume of the helium bottle. At atmospheric pressure p_{atm}, Δn corresponds to a helium volume of

$$V = \frac{\Delta n RT}{p_{atm}} = \frac{\Delta p V_{bottle}}{p_{atm}} \tag{5.17}$$

Here, it was assumed that the temperature of the helium doesn't change when it streams out of the bottle.
The helium volume flow Q is given by

$$Q = \frac{V}{t} \tag{5.18}$$

and the flow velocity by

$$v = \frac{Q}{A} \tag{5.19}$$

where A is the cross-section area of the flow. In this case, it is the cross-section area of the anemometer, which is $A = \pi(3.5\,\mathrm{cm})^2 \approx 38.5\,\mathrm{cm}^2$.

measurement	v_{uncal} [m/s]	t [s]	Q [m^3/s]	v_{cal} [m/s]
1	1.45 ± 0.1	200	$(2.5 \pm 0.5)10^{-3}$	0.65 ± 0.13
2	1.55 ± 0.1	142	$(3.5 \pm 0.7)10^{-3}$	0.91 ± 0.18
3	1.90 ± 0.1	180	$(2.8 \pm 0.6)10^{-3}$	0.72 ± 0.14
4	2.15 ± 0.1	160	$(3.1 \pm 0.6)10^{-3}$	0.81 ± 0.16
5	2.24 ± 0.1	100	$(5.0 \pm 1.0)10^{-3}$	1.30 ± 0.26
6	2.35 ± 0.1	97	$(5.2 \pm 1.0)10^{-3}$	1.34 ± 0.27
7	2.65 ± 0.1	100	$(5.0 \pm 1.0)10^{-3}$	1.30 ± 0.26
8	2.89 ± 0.1	90	$(5.7 \pm 1.1)10^{-3}$	1.44 ± 0.29

Table 5.1: *Data used to calibrate the anemometer for helium*

This method clearly has large uncertainties. The hose that connects the pressure regulator with the diffusor has a cross-section area $A_{hose} = \pi(0.2\,\text{cm})^2 \approx 0.13\,\text{cm}^2$. This is very small compared to the anemometer cross-section area A. According to (5.19), the flow velocities in the hose are $\frac{A}{A_{hose}} \approx 300$ times larger than in the anemometer (assuming incompressible flow). In this regime, one can no longer assume laminar flow. Additionally, non-laminar effects are expected due to the diffusor not being ideal. This is illustrated in figure 5.9. The effects lead to energy dissipation, which results in uncertainties that cannot be accounted for at this point.

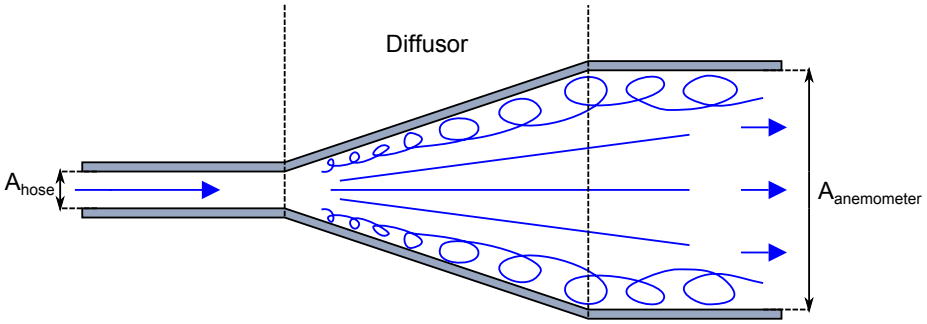

Figure 5.9: *Schematic of a diffusor*

An uncertainty that can be accounted for is the reading error of the pressure difference. It was estimated to be 20 %. Accordingly, the relative error of the volume V is also 20 %. The data that was taken for the calibration is shown in table 5.1. v_{uncal} is the velocity that was read off the uncalibrated anemometer and v_{cal} is the velocitiy that was calculated from the data, using (5.18) and (5.19).
Figure 5.10 shows v_{cal} plotted against v_{uncal} and a straight line fit with fixed point (0,0), which represents the calibration curve.
The maximum flow velocity that could be reached by fully turning up the pressure reducer on the helium bottle is $v_{uncal} \approx 2.9\,\frac{\text{m}}{\text{s}}$. The maximum v_{uncal} measured during the cooling tests was approximately $5\,\frac{\text{m}}{\text{s}}$. Therefore, the calibration curve has to be extrapolated.
The only fit parameter is the slope $b = 0.46 \pm 0.03$. The calibration yields

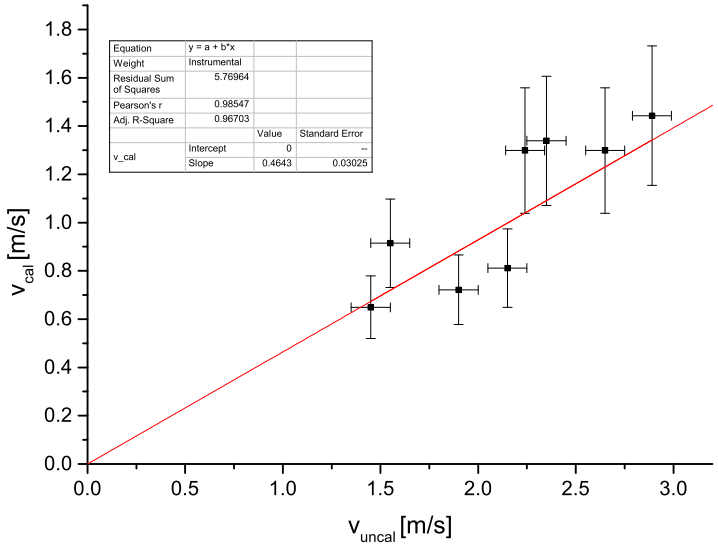

Figure 5.10: *Straight line fit to v_{cal} vs. v_{uncal} to calibrate the anemometer for helium*

$$v_{cal} = 0.46 \cdot v_{uncal} \tag{5.20}$$

and

$$\Delta v_{cal} = \sqrt{(v_{uncal}\Delta b)^2 + (b\Delta v_{uncal})^2} \tag{5.21}$$

where $\Delta b = 0.03$, and $\Delta v_{uncal} = 0.1\,\frac{\mathrm{m}}{\mathrm{s}}$ is the same error as for the air flow velocity.

5.3.5 Full-Scale Model of One Detector Station

The first heatable detector model, which the Mu3e cooling concept was tested with, is a full-scale model of the complete layers 3 and 4 of one detector station. It is approximately 40 cm long and has a diameter of about 16 cm. The distance between the two layers is approximately 1 cm. The model consists of 25 µm thin aluminum foil laminated on 25 µm thin Kapton® polyimide film. For ease of production, the detector geometry of one 24-sided and one 28-sided prism has been changed to two cylinder barrels. Each of the two cylindrical layers is divided into four segments. The size of a segment is 40 cm × 13 cm for layer 4 and 40 cm × 11 cm for layer 3. The segments are glued on a 3D-printed support structure (see figure 5.12) with two-component epoxy adhesive, which is temperature resistant up to 200 °C at least over short time periods.
The support structure is screwed to aluminum end rings to place the model in the center of the flow channel. Each of the eight layer segments is connected to a separate channel of a power supply. Since the electrical connectors are too

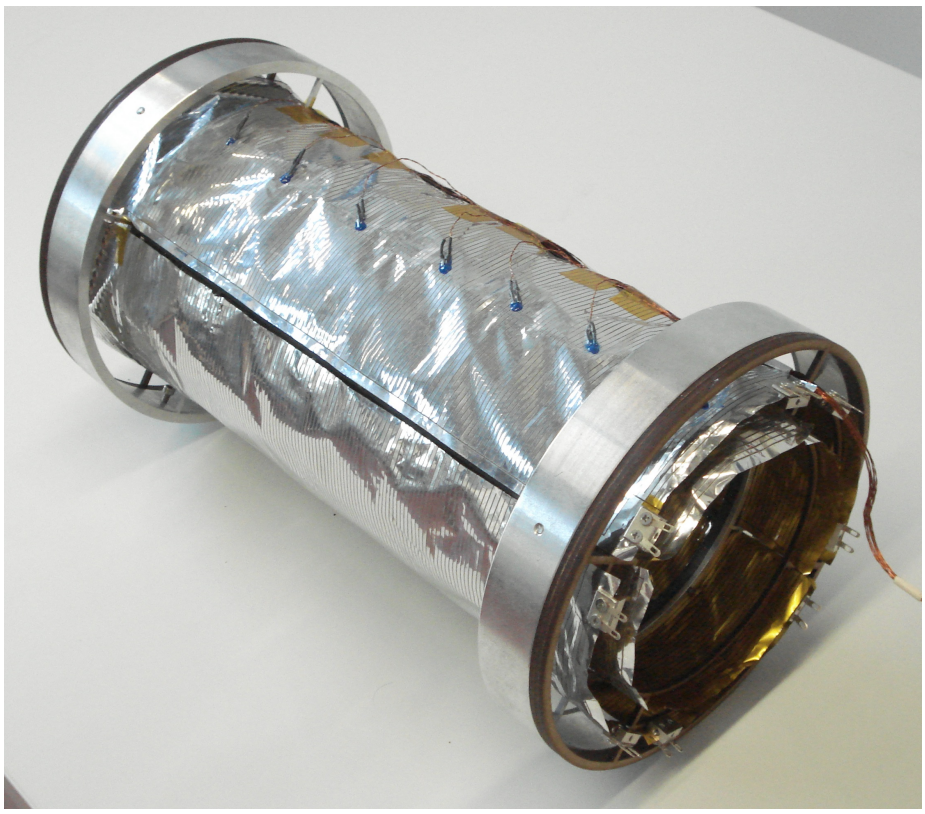

Figure 5.11: *Photo of the full-scale model of one detector station*

heavy to be carried by the foil alone, a wooden support frame was glued on the aluminum endrings for stress relief. Pt1000 temperature sensors were glued on the model with thermally conductive adhesive (eight sensors on layer 4 and four sensors on layer 3). On both layers, they are placed in line with the symmetry axis of the model. To reach heating powers that are comparable with that of the real detector, it was necessary to increase the ohmic resistance of the layer segments (see next page). This was done by laser cutting the pattern shown in figure 5.13 into the aluminum without destroying the Kapton® foil. The pattern not only increases the resistivity of the segments, but it also allows for heating them uniformly.
A more detailed description of the production of this detector model can be found in [27].
First experiments were carried out, where the temperatures on the model were measured while it was heated and, at the same time, cooled by an air flow. The measurement was performed for different heating powers and different air flow velocities.
Table 5.2 shows the total heating power of the full model, per layer, and per segment, depending on the heating power per surface area P/A. The pattern shown in figure 5.13 was designed such that a heating power of $P/A = 150\,\mathrm{mW/cm^2}$ could be reached by applying reasonable voltages to the individual segments.
To estimate the required supply voltage for a segment, depending on the width

Figure 5.12: *Photo of the 3D-printed support structure with three segments of layer 3 glued to it*

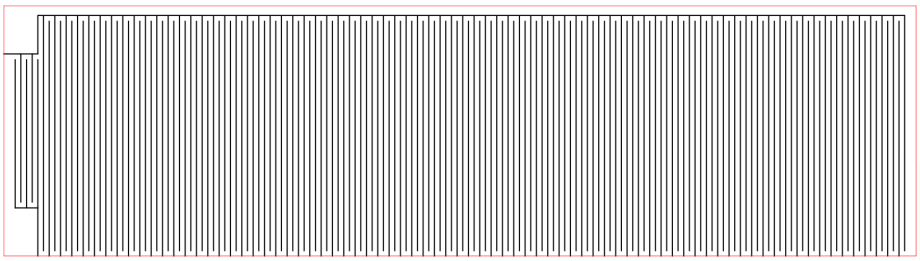

Figure 5.13: *Heating pattern for one segment of layer 3 (40 cm long, 11 cm wide)*

of the conducting traces of the heating pattern, the following calculations were made.
The pattern has roughly 150 traces. The space between two traces is 0.5 mm wide. The single horizontal trace at the top of the pattern as well as the left part with a width of 15 mm, which includes the spaces for the electrical connectors, was neglected. The remaining pattern is of the size 385 mm × 125 mm (for layer 4). The trace is then approximately $d = 2\,\text{mm}$. The behaviour of the current in the reversal points is not taken into account. Instead, simply one single trace of the length $l = 150 \cdot 125\,\text{mm}$ is assumed. The aluminum has a thickness $h = 0.025\,\text{mm}$. The resistance of the segment is given by:

$$R = \rho_{Al} \cdot \frac{l}{A_t} \tag{5.22}$$

where ρ_{Al} is the electrical resistivity of aluminum and $A_t = d \cdot h$ is the cross-

P/A [mW/cm^2]	$P_{Segment}$ [W]		P_{Layer} [W]		P_{total} [W]
	layer 3	layer 4	layer 3	layer 4	
100	44	52	176	208	384
150	66	78	264	312	576
250	110	130	440	520	960
400	176	208	704	832	1536

Table 5.2: *Heating power of the full model, per segment, and per layer for different values of heating power per surface area P/A*

section area of the traces. With $\rho_{Al} = 2.82 \cdot 10^{-8}\,\Omega$m (at 20 °C) one gets $R \approx 10.6\,\Omega$.
The resistances of the real segments were measured to be between 13.0 Ω and 13.8 Ω for layer 4 and between 11.9 Ω and 12.1 Ω for layer 3 at 20 °C.

With the equations

$$U = RI \tag{5.23}$$

and

$$P = UI \tag{5.24}$$

the voltage and current needed to heat a segment with a certain heating power per surface area can be calculated. To heat for example a segment of layer 4 ($R = 13.8\,\Omega$) with $P/A = 150\,\mathrm{mW/cm^2}$ (see table 5.2 for according total power P), one needs a supply voltage of

$$U = \sqrt{PR} \approx 32.8\,\mathrm{V} \tag{5.25}$$

and the corresponding current is

$$I = \sqrt{\frac{P}{R}} \approx 2.4\,\mathrm{A} \tag{5.26}$$

The resistance changes with temperature, but the supply voltage doesn't have to be calculated exactly, because the power consumption can be directly read off the power supplies that were used in the experiment[3].

Results of the Cooling Tests with Air

In the following, the results of the measurements with the setup described above are presented. Figures 5.14 and 5.15 show the temperature profiles along the detector model measured ontop of layer 4 for heating powers of $P/A = 100\,\mathrm{mW/cm^2}$ and $150\,\mathrm{mW/cm^2}$ and different air flow velocities.
The horizontal axis gives the positions of the temperature sensors along the detector model. The air flow is coming from the right. On the vertical axis, the temperature ΔT is plotted. ΔT denotes the difference between the measured temperature T and the temperature of the incoming coolant T_0:

[3] HAMEG HMP 4040

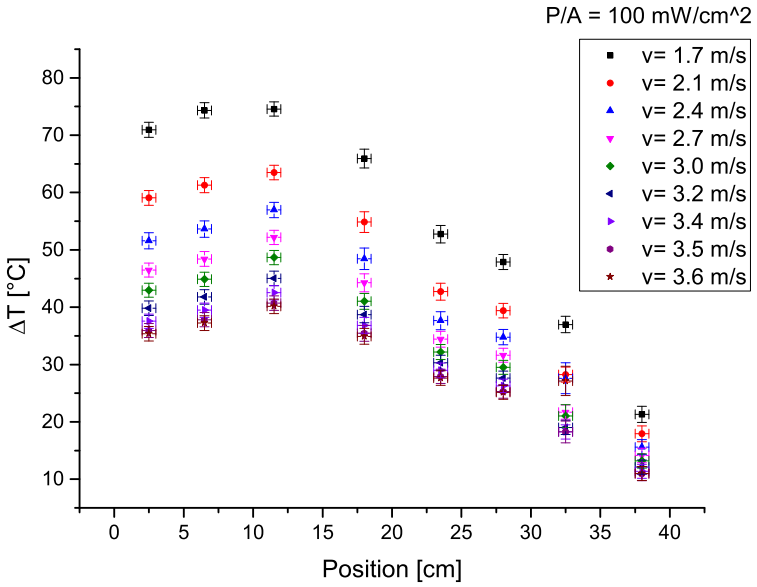

Figure 5.14: *Temperature profiles for different air flow velocities at* $P/A = 100\,mW/cm^2$

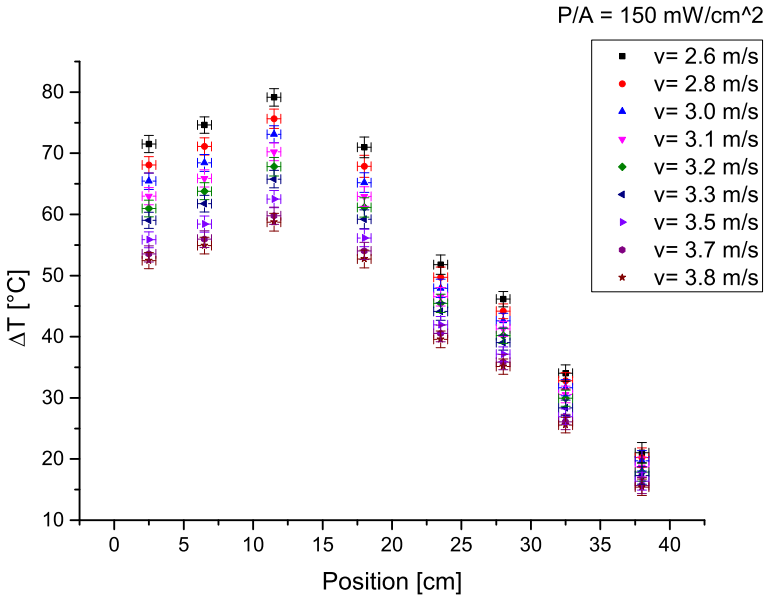

Figure 5.15: *Temperature profiles for different air flow velocities at* $P/A = 150\,mW/cm^2$

$$\Delta T = T - T_0 \tag{5.27}$$

T_0 corresponds to the temperature in the lab, since the coolant is the ambient air. The air conditiong in the lab is always set to 20 °C. To monitor small changes in T_0, it is measured at the input side of the flow channel with the anemometer, which includes a thermometer. ΔT is the quantity of interest, instead of T, because for the Mu3e experiment, the temperature of the coolant will be slightly above 0 °C to keep the maximum temperature as low as possible while still preventing water, which might accidentally enter the detector, from freezing. The measurement was carried out with different air flow velocities ranging from 1.7 $\frac{\mathrm{m}}{\mathrm{s}}$ to 3.8 $\frac{\mathrm{m}}{\mathrm{s}}$. The flow velocity was adjusted by varying the supply voltage of the fans that create the air flow. The upper limit of the velocity range was set only by the used power supply. It could, in principle, be increased further.
As expected (see section 5.1), the temperature first increases along the detector model in flow direction with decreasing gradient. The temperature reaches its maximum not exactly at the end of the detector model but approximately 10 cm in front of it, before it decreases again. This effect is discussed in section 5.4, where the measured profiles are compared with the results of CFD simulations. As expected, the temperature decreases overall with increasing air flow velocity. The errors on ΔT, here and throughout the rest of this thesis, consist of a statistical error ΔT_{stat} due to fluctuations of the single measurements, given by the standard deviation $\sigma_{\Delta T}$, which is typically of the order of 0.1°C, and a calibration error $\Delta T_{cal} = 1\,°\mathrm{C}$ (see section 5.3.3):

$$\Delta(\Delta T) = \Delta T_{stat} + \Delta T_{cal} \tag{5.28}$$

Figures 5.16 and 5.17 show the peak temperature on the detector model ΔT_{max} plotted against the flow velocity, again for $P/A = 100\,\mathrm{mW/cm^2}$ and $150\,\mathrm{mW/cm^2}$, respectively. In both plots, the function

$$y(x) = A + B \cdot \frac{1}{\sqrt{x}} \tag{5.29}$$

with fit parameters A and B was fitted to the data, according to (5.10), which is derived in section 5.1. The offset A was added, because otherwise the fit would not match the data. The reason for that could be that the data has to approach a finite temperature value for $v \to 0\,\frac{\mathrm{m}}{\mathrm{s}}$ because of heat dissipation by thermal radiation, but (5.10) does not account for that. Instead, according to (5.10), ΔT_{max} goes to infinity for $v \to 0\,\frac{\mathrm{m}}{\mathrm{s}}$. This might result in a negative offset A of the fit.
The MuPix prototypes have been tested to show an acceptable signal-to-noise ratio up to operating temperatures of 70 °C (see 5.2). So, according to these measurements, for a single detector station of the length of about 40 cm, layers 3 and 4 could already be sufficiently cooled with a global air flow of a velocitiy of $v_{air} \approx 3\,\frac{\mathrm{m}}{\mathrm{s}}$ at $P/A = 150\,\mathrm{mW/cm^2}$.

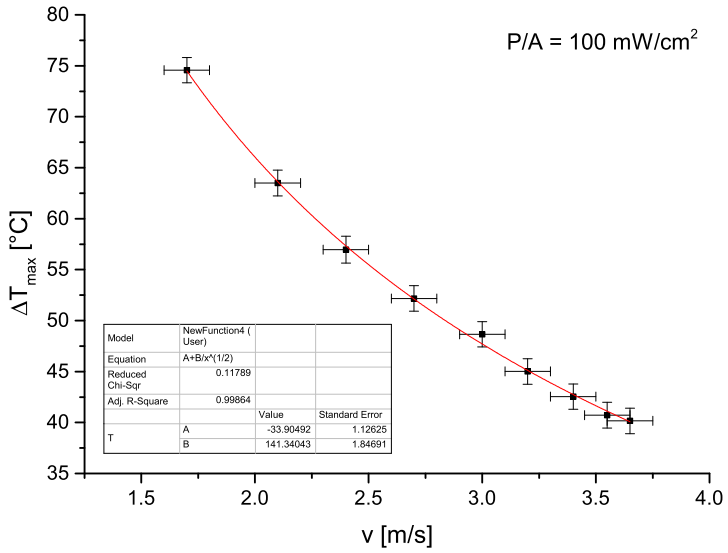

Figure 5.16: *ΔT_{max} plotted against the air flow velocity at $P/A = 100\,mW/cm^2$*

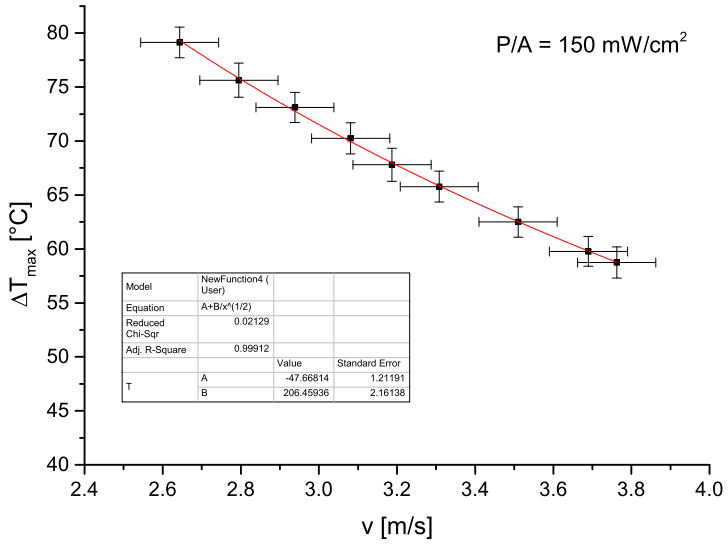

Figure 5.17: *ΔT_{max} plotted against the air flow velocity at $P/A = 150\,mW/cm^2$*

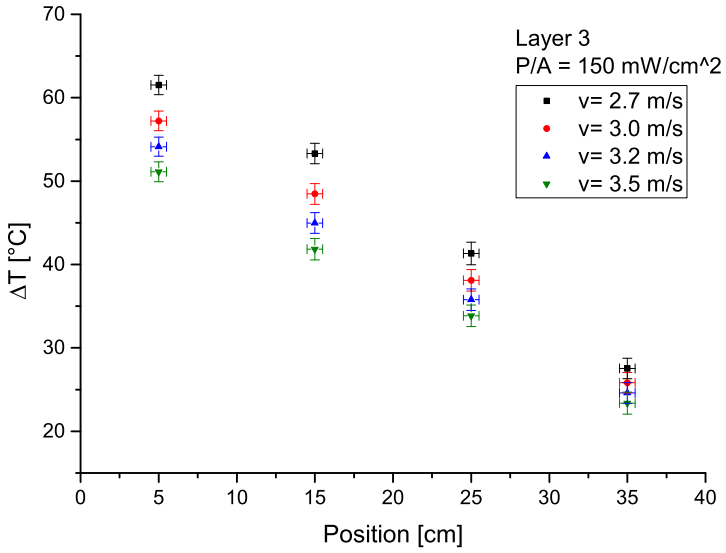

Figure 5.18: *Temperature profiles on layer 3 for different air flow velocities at* $P/A = 150\,mW/cm^2$

Temperature profiles were also measured for layer 3. The results are shown in figure 5.18. Here, the actual maximum temperature might not be observable, because layer 3 is equipped with only four temperature sensors instead of eight. Therefore, the result might be biased because of too little coverage. A comparison of the profiles of layers 3 and 4 is shown in figure 5.19. Overall, the maximum measured temperature of layer 3 never exceeds that of layer 4, as shown in figure 5.20. For this plot, the temperatures on both layers were measured simultaneously with four temperature sensors each.
It was also tested, if there was a significant temperature variation in vertical direction. During the measurements discussed above, the temperature sensors were placed at the top of the detector model. For this measurement, the whole model was rotated around the cylinder axis by 90° and 180°, such that the temperature sensors were located at the side and at the bottom of the model, respectively. The results are shown in figure 5.21 . As one can see, the temperatures at the bottom are up to 5 °C lower than at the side and the top. This can be explained by natural convection. Since it is the highest occuring temperature that is of interest, all temperature measurements discussed in the following were taken at the top of the detector model.

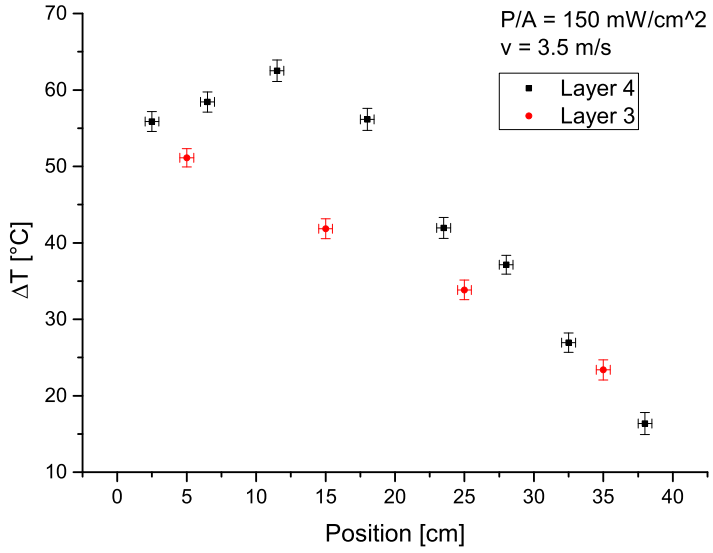

Figure 5.19: *Comparison of the temperature profiles on layer 3 and layer 4 for an air flow velocity* $v = 3.5\,\frac{m}{s}$ *and* $P/A = 150\,mW/cm^2$

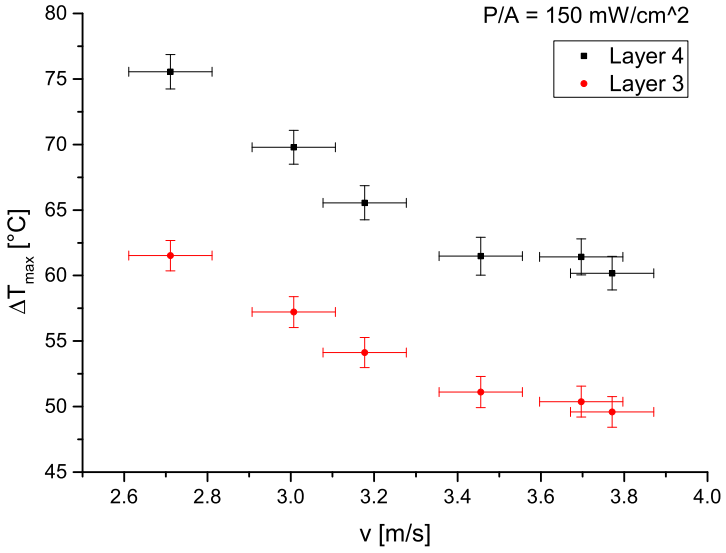

Figure 5.20: ΔT_{max} *plotted against the air flow velocity* v *for layers 3 and 4*

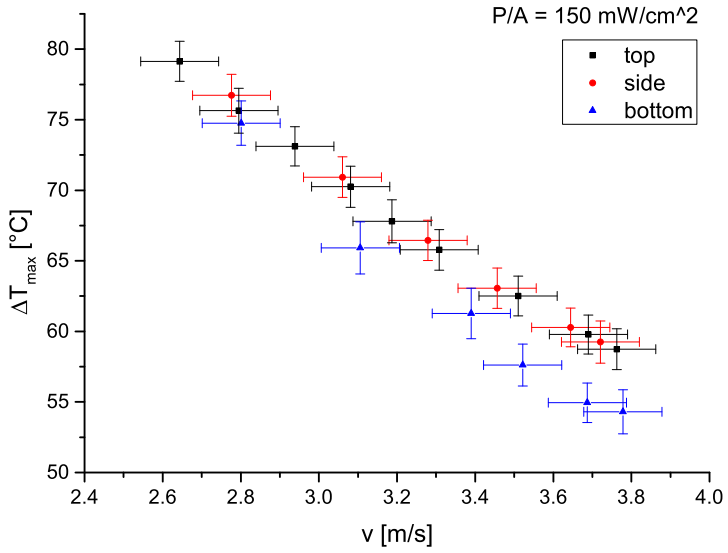

Figure 5.21: *ΔT_{max} measured at the top, the side, and the bottom of the detector model plotted against the flow velocity*

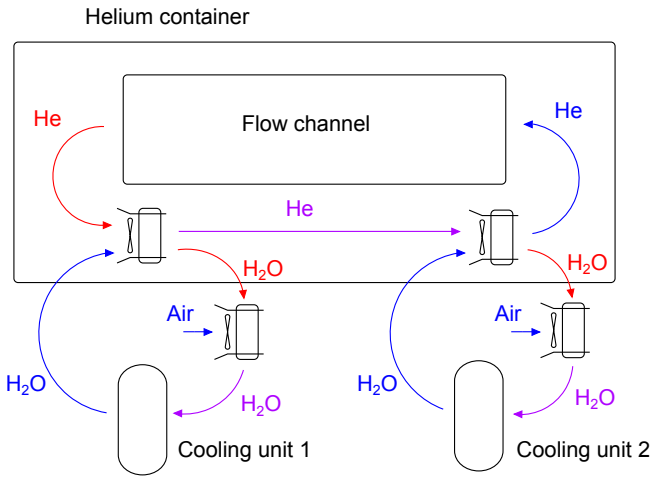

Figure 5.22: *Schematic of the setup for helium cooling tests*

5.3.6 Helium Cooling

The tests discussed above were all done with air as coolant, instead of helium. To test the cooling with helium, the experiment was repeated with a modified setup placed in a helium atmosphere. The latter was realized by putting a plastic box ontop of the flow channel and filling it with helium. Therefore, the experiment took place inside a finite helium volume of roughly 250 l. Since there was a heat source inside this volume, additional cooling was required. It was realised by a water cooling system, consisting of two lab cooling units with roughly 100 W cooling power each. They were located ouside the helium container, and radiators with fans, designed for PC water cooling, were placed inside the helium container (see figure 5.22). Since the combined heating power of both cooling units was not enough to cool away a heating power of $150\,\mathrm{mW/cm^2}$, additional radiators were placed outside the helium container to precool the water with the 20 °C warm ambient air in the lab, before it re-entered the cooling units. Still the heating power had to be reduced to $100\,\mathrm{mW/cm^2}$ to sustain a constant helium temperature at a reasonable level ($T_0 < 30\,°\mathrm{C}$)[4].

Measurement of the Helium Concentration

To measure the effect of helium as coolant, compared to air, one needs to know the helium concentration in the container. To determine it, a setup was constructed to measure the speed of sound inside the helium container. The speed of sound depends on the medium and, in case of a mixture of gases, on the concentrations of the different components. For gas, the speed of sound c is approximately given by

$$c = \sqrt{\gamma \cdot \frac{p}{\rho}} \tag{5.30}$$

with the pressure p, the gas density ρ and the adiabatic index $\gamma = \frac{c_p}{c_v}$, where c_p and c_v are the specific heat capacities at constant pressure and constatnt

[4] measured at the input side of the flow channel

volume, respectively.
For a mixture of two gases, one has to insert a total pressure

$$p = p_1 + p_2 \tag{5.31}$$

as well as an average ρ and an average γ:

$$\rho = \frac{m}{V} \tag{5.32}$$

with $m = m_1 + m_2$ and m_i being the absolute masses of the gases contained in the volume V.

$$\gamma = \frac{c_p}{c_v} = \frac{\frac{m_1}{m}c_{p,1} + \frac{m_2}{m}c_{p,2}}{\frac{m_1}{m}c_{v,1} + \frac{m_2}{m}c_{v,2}} = \frac{m_1 c_{p,1} + m_2 c_{p,2}}{m_1 c_{v,1} + m_2 c_{v,2}} \tag{5.33}$$

In the following, the above quantities are expressed in terms of the teperature T, the volume V, the gas constant $R = 8.314\,\frac{\mathrm{J}}{\mathrm{mol}\cdot\mathrm{K}}$, the molar masses M_i and the amounts of substance $n_i = \frac{m_i}{M_i}$ $(i = 1, 2)$.

$$\rho = \frac{n_1 M_1 + n_2 M_2}{V} \tag{5.34}$$

With (5.31) and the ideal gas equation (5.15) one gets:

$$p = \frac{RT}{V}(n_1 + n_2) \tag{5.35}$$

From (5.33) one gets:

$$\gamma = \frac{n_1 M_1 c_{p,1} + m_2 M_2 c_{p,2}}{n_1 M_1 c_{v,1} + m_2 M_2 c_{v,2}} \tag{5.36}$$

Now let x be the substance amount fraction of gas 1:

$$x \equiv \frac{n_1}{n_1 + n_2} \tag{5.37}$$

Then n_2 is given by

$$n_2 = \frac{1 - x}{x} n_1 \tag{5.38}$$

Inserting (5.34) to (5.38) into the general expression (5.30) gives

$$c = \sqrt{\frac{M_1 c_{p,1} + \frac{1-x}{x} M_2 c_{p,2}}{M_1 c_{v,1} + \frac{1-x}{x} M_2 c_{v,2}} \cdot \frac{RT}{xM_1 + (1-x)M_2}} \tag{5.39}$$

Now 1 shall be indentified with helium and 2 with (dry) air. In table 5.3, the according values for M, c_v and c_p at standard conditions (298.15 K, 10^5 Pa) are summarized.
Figure 5.23 shows c plotted against the helium concentration x according to (5.39), with the values from table 5.3 inserted and $T = 293.15\,\mathrm{K}$. Figure 5.24 shows the inverse function, with wich the helium concentration can be calculated if the speed of sound is known.

gas	M_{He} [kg/mol]	c_p [J/(mol·K)]	c_v [J/(mol·K)]
air	$28.949 \cdot 10^{-3}$	$1.005 \cdot 10^3$	$0.718 \cdot 10^3$
helium	$4.003 \cdot 10^{-3}$	$5.193 \cdot 10^3$	$3.116 \cdot 10^3$

Table 5.3: *Literature values for calculating the speed of sound in a mixture of air and helium*

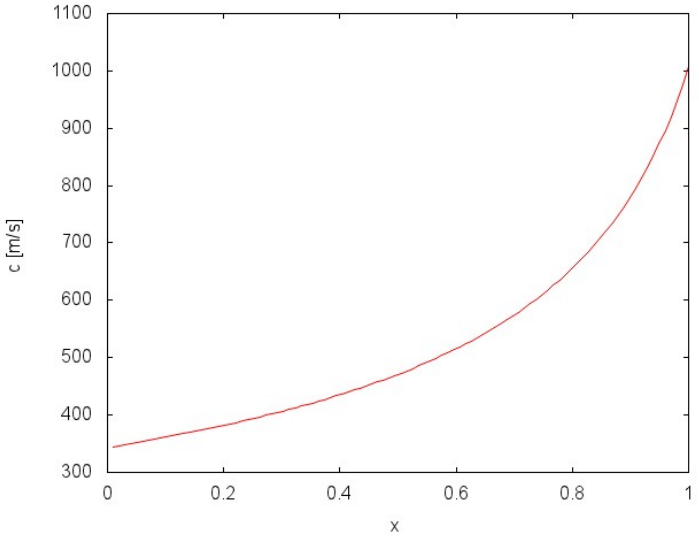

Figure 5.23: *Speed of sound c in a mixture of air and helium plotted against the helium concentration x*

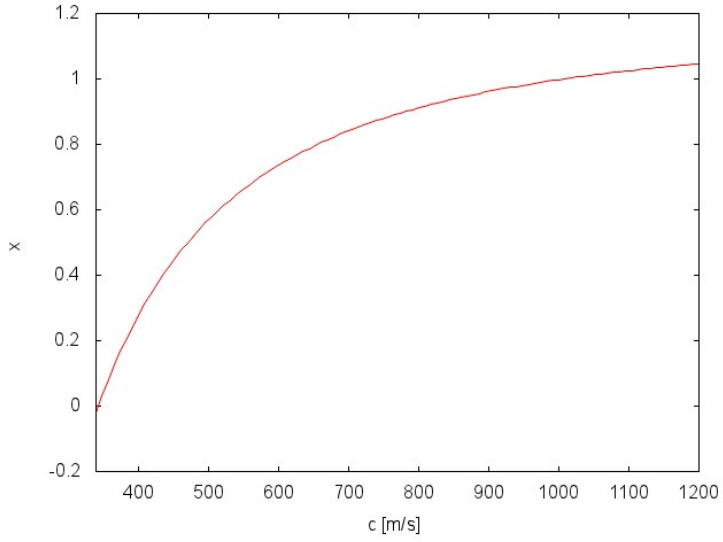

Figure 5.24: *Helium concentration x in a mixture of air and helium as function of the speed of sound c*

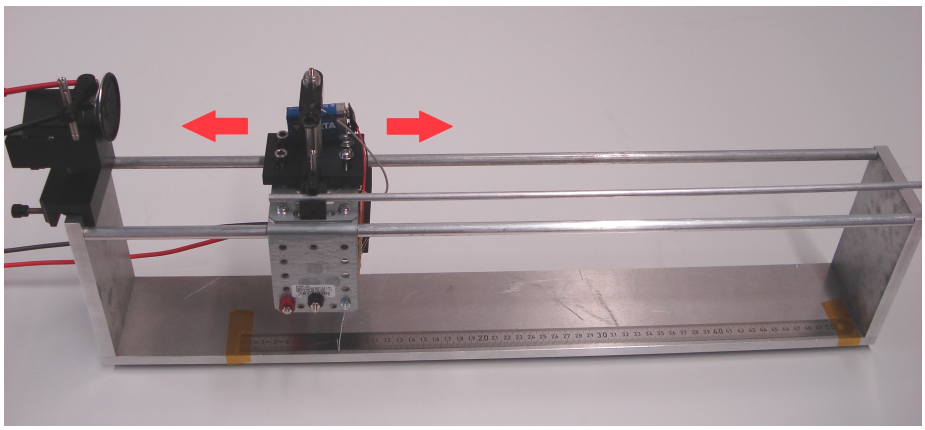

Figure 5.25: *Setup for measuring the speed of sound consisting of a loudspeaker and a receiver on a slider*

Measurement of the Speed of Sound via Sonic Travel Time

To measure the speed of sound, the setup shown in figure 5.25 was placed inside the helium container. It consists of a slider on a double rail, which carries a microphone and an amplifier, and a loudspeaker fixed to the rails. A function generator outputs a sine signal with a frequency $f = 10\,\mathrm{kHz}$, which is split into two signals. Once, the signal is directly transmitted to an oscillocope (signal 1). The other signal (signal 2) is also transmitted to the oscilloscope, but it travels through the system of transmitter and receiver first. Figure 5.26 shows an according schematic.

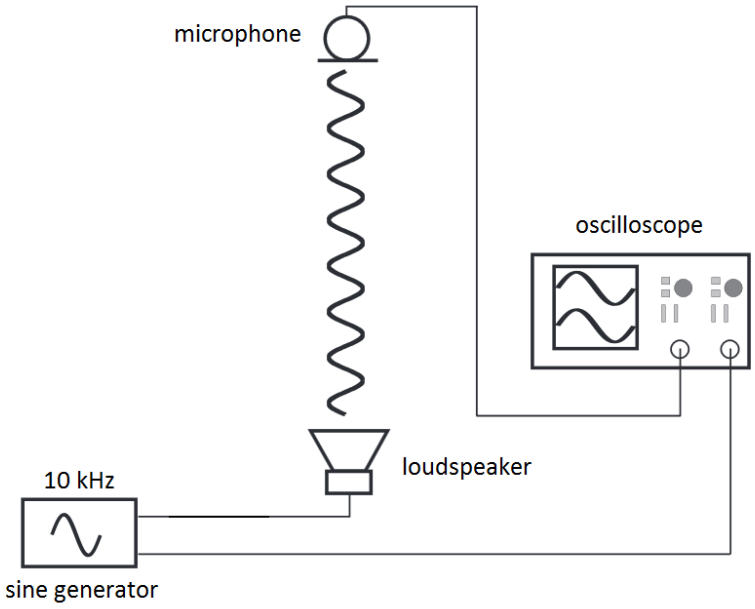

Figure 5.26: *Schematic of the setup for the speed of sound measurement [33]*

The setup allows for varying the distance between transmitter and receiver manually from outside the helium container via an arm. By doing this, one varies the distance that the sound wave travels inside the medium between transmitter and receiver and therefore the travel time. On the oscilloscope, if one triggers on signal 1, one can see signal 2 moving relatively to it, when moving the receiver. If one moves signal 2 exactly by n periods relative to signal 1, where n is an integer, and measures the distance d, by which the receiver is moved, one can calculate the speed of sound simply via

$$c = \lambda f \tag{5.40}$$

where the wavelength λ is given by $\lambda = \frac{d}{n}$. The error Δc is determined by the error of the distance measurement Δd:

$$\Delta c = \frac{\Delta d}{n} f \tag{5.41}$$

There is a length scale fixed to the rails to determine d by measuring the position of the slider before and after moving it. For each measurement, a reading error of 0.5 cm is estimated, which gives a total error $\Delta d = \sqrt{2 \cdot (0.5\,\text{cm})^2} \approx 0.7\,\text{cm}$. One problem that occured during this measurement was that, inside the helium container, interferences with reflected soundwaves occured, such that one could not observe a clean sine for signal 2 anymore. Therefore, the helium container was partly lined with foam material (see figure 5.27). This didn't solve the problem entirely, but it made measurements possible.
A test measurement was carried out without helium in the container (at $T = 20\,^\circ\text{C}$). The results are summarized in table 5.4. The average is $c = 352\,\frac{\text{m}}{\text{s}}$, and the standard deviation is $\sigma = 5\,\frac{\text{m}}{\text{s}}$. The literature value for the speed of sound in air is $c_{literature} = 343\,\frac{\text{m}}{\text{s}}$. Taking into account the reading error $\Delta c = \frac{\Delta d}{n} \cdot f = 14\,\frac{\text{m}}{\text{s}}$, the measurement is in good agreement with the literature.

n	d [cm]	λ [cm]	c [m/s]
5	17.6	3.52	352
5	17.7	3.54	354
5	17.6	3.52	352
5	17.2	3.44	344
5	17.8	3.56	356

Table 5.4: *Results of test measurement of the speed of sound in air*

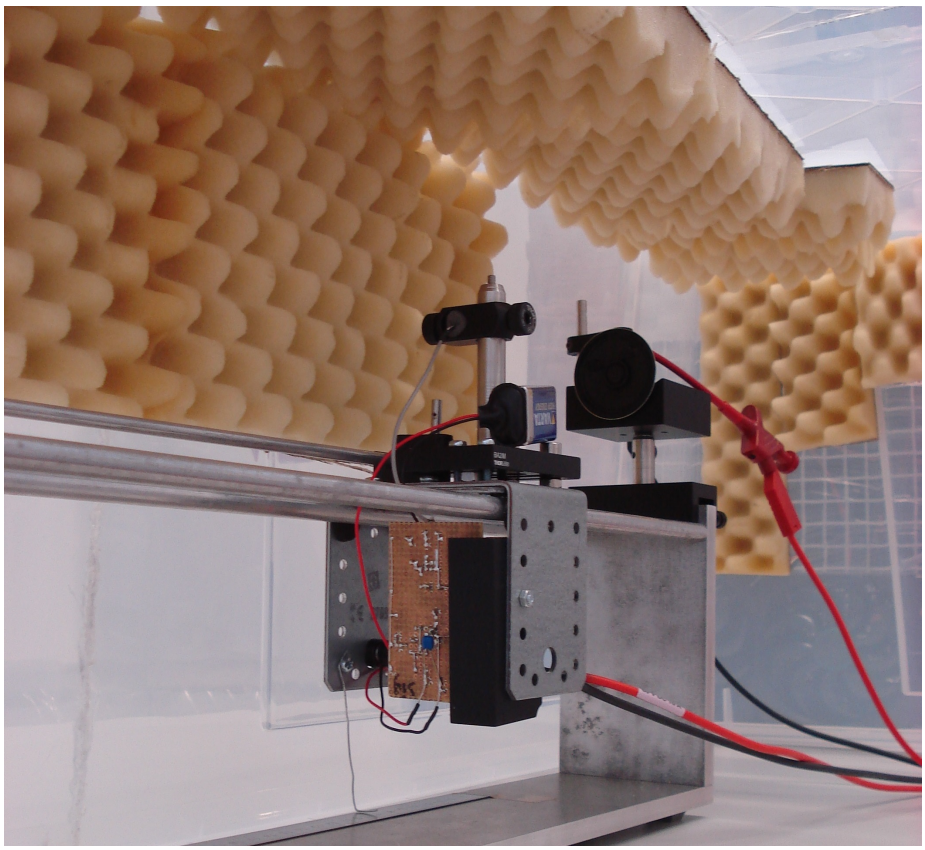

Figure 5.27: *Photo of the setup for measuring the speed of sound taken inside the helium container showing the lining*

Containment of the Helium

To minimize the helium loss through gaps between the helium container and the table, as well as at the cable lead-throughs, the gaps were sealed with elastic sealing compound. To test how well the helium can be contained, the container was filled with helium, then the helium supply was turned off, and the helium concentration was monitored over time. The results are shown in figure 5.28. One can see that the container can be filled with approximately 100 % of helium, but after switching off the helium supply, the concentration decreases fast (half-life of ≈ 89 min, assuming exponential decay). Unfortunately, the helium concentration measurement cannot be carried out while the helium supply is turned on, or while the fans inside the container are running. In both cases, too much background noise is produced, which distorts the signal received by the microphone. Therefore, the helium concentration cannot be monitored during the cooling tests. Consequently, the helium supply stays always turned on during measurements, just as much as it is required to compensate for the helium loss. For all measurements discussed in the following, the helium concentration was assumed to be 100 %.

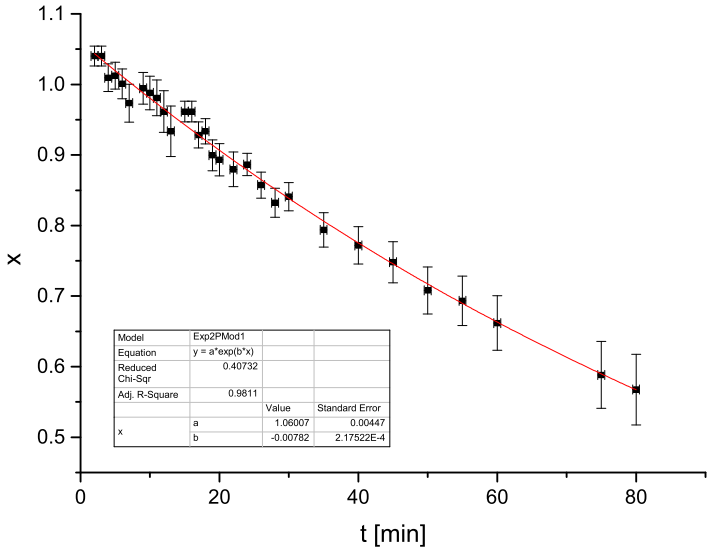

Figure 5.28: *Helium concentration x plotted against time t after turning off the helium supply*

Results of the Cooling Tests with Helium

The results of the cooling tests with helium are shown in figure 5.29, where ΔT_{max} is plotted against the flow velocity v. For comparison, the according results of the cooling tests with air described above were also plotted again. To compare the results of the cooling tests with air and helium, it was necessary to measure the helium flow velocity. This was done in the way described in section 5.3.4. Although this method may introduce unknown errors, the results are in good agreement with the corresponding CFD simulations presented in section 5.4. In figure 5.46, the data from figure 5.29 is plotted again together with the results of the corresponding simulations for comparison.
As expected, the cooling performance is better for helium than for air (see section 5.1). In the flow velocity regime where both measurements overlap, i.e. between 1.7 and 2.6 $\frac{\mathrm{m}}{\mathrm{s}}$, ΔT_{max} is approximately twice as large for air as for helium. This corresponds to differences in ΔT_{max} between helium and air of 30 to 40 °C.

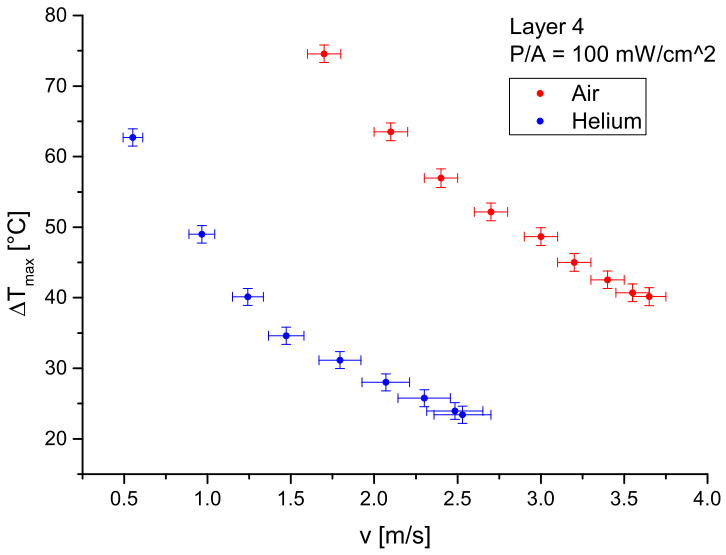

Figure 5.29: *ΔT_{max} plotted against the flow velocity for air and helium at $P/A = 100\,mW/cm^2$*

5.3.7 Heatable Module Prototypes and Local Cooling

Further cooling tests were carried out with a different heatable detector model, which consits of ohmically heatable module prototypes. It should be pointed out that this model does not include the complete detector layers like the one discussed above, but it only represents a cutout of layers 3 and 4 of one detector station. In return, this cutout has a geometry similar to that of the real detector. The module prototypes resemble those described in section 4.2.3 and were built with the same tools. The support structure consists of a laminate of 25 µm thin Kapton® film and 12 µm thin aluminum foil, and it has prism shaped folds to increase the mechanical stability of the module, as discussed in section 4.2.3. The folds can also be used for cooling purposes, which is discussed below in this section. Between the support structure and each row of glass plates, which represent the silicon sensors, there is a stripe of the same aluminum-Kapton® laminate that was used for the support structure. The stripes represent the flex-prints for power and signal lines, and, in this case, they also allow for heating the module prototypes for cooling tests. Therefore, a pattern was cut into the aluminum part of the laminate with a laser cutter, like for the detector model discussed in the previous sections. The pattern is shown in figure 5.30.

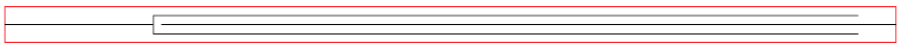

Figure 5.30: *Heating pattern for one stripe of a detector module prototype*

One stripe has a resistance of approximately 1 Ω, is 1.8 cm wide, and has a length of 45 cm to leave enough space for electrical connectors, while the rest of the module is only 39 cm long, including the plastic endpieces.
One module has four sides. Since layer 3 (4) has 24 (28) sides, a module represents $\frac{1}{6}$ ($\frac{1}{7}$) of the full layer.
For not having to connect each heating stripe to a power supply separately, the four stripes of one module are interconnected by metal plates, which were attached via ultrasonic soldering. This way, one module can be connected to one channel of a power supply (see figure 5.31).

Local Cooling

The cooling tests discussed above were carried out with a model of only one detector station. It was shown that, by cooling with a global helium flow with a velocity of $v_{He} \approx 2.5 \frac{\mathrm{m}}{\mathrm{s}}$, a maximum temperature ΔT_{max} of 25 °C can be reached. But considering that the final phase II detector will be five times as long, it is expected that cooling with a global flow alone will not be sufficient. Furthermore, it will not be possible to establish a global flow inside the detector stations, because the beampipe, the electronics, and the services will block the vent. Therefore, it is planned to complement the global helium cooling by a so-called "local" cooling system, which allows for supplying helium to each detector station separately.
For this purpose, a gas distribution system is integrated in the module endpieces and the station endrings, to which helium can be guided via pipes or hoses through the inactive parts of the detector, i.e. the inside of the recurl stations.

Figure 5.31: *Electriacal connections of the heating stripes of one module attached via ultrasonic soldering*

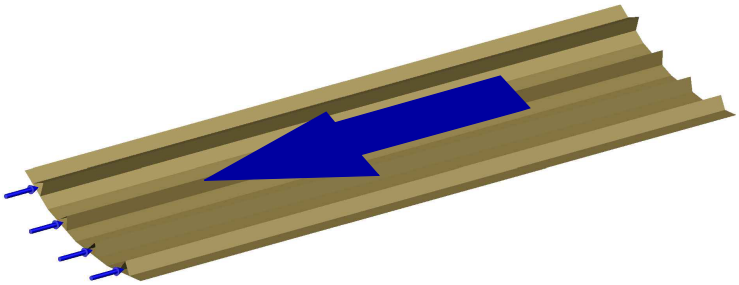

Figure 5.32: *Illustration of the cooling of a mudule from both sides*

In addition to guiding the helium out via the module endpieces in the direction of the global flow and having it mix with the latter, there is another possibility, offered by the prism shaped folds in the module support structure. The folds form channels, inside of which an additional helium flow can be applied. Since this flow is isolated from the global flow, it can be directed oppositely to the latter. The detector stations can therefore be cooled from both sides simultaneously (see figure 5.32). Considering the temperature profiles presented in section 5.3.5, this should lead to an additional improvement of the cooling

performance. In the following, the helium flow inside the cooling channels is referred to as local flow.

Cooling Tests with Heatable Module Prototypes

For cooling tests with heatable module prototypes, the setup for the helium cooling tests discussed in section 5.3.6 is used, only with the detector model exchanged, and with additional hoses for distributing the local helium flow, and a flowmeter for measuring the local helium flow velocity. The new model has the length of one detector station. The module prototypes are mounted to aluminum endrings and are supported by a 3D-printed support frame. Parts of the latter had to be cut away to make room for the modules. Each module is connected to one channel of a power supply. The helium for the local flow is distributed via silicone hoses that connect the inlet of the module endpieces to a lead-through in the flow channel. For he cooling tests, an older mechanical design is used, where the gas distribution system is not yet integrated in the station endring, but an additional piece for each end of a module is needed, which is shown in figure 5.33. Figure 5.34 shows the detector model placed in the flow channel and figure 5.35 shows part of a module prototype with temperature sensors glued on it.

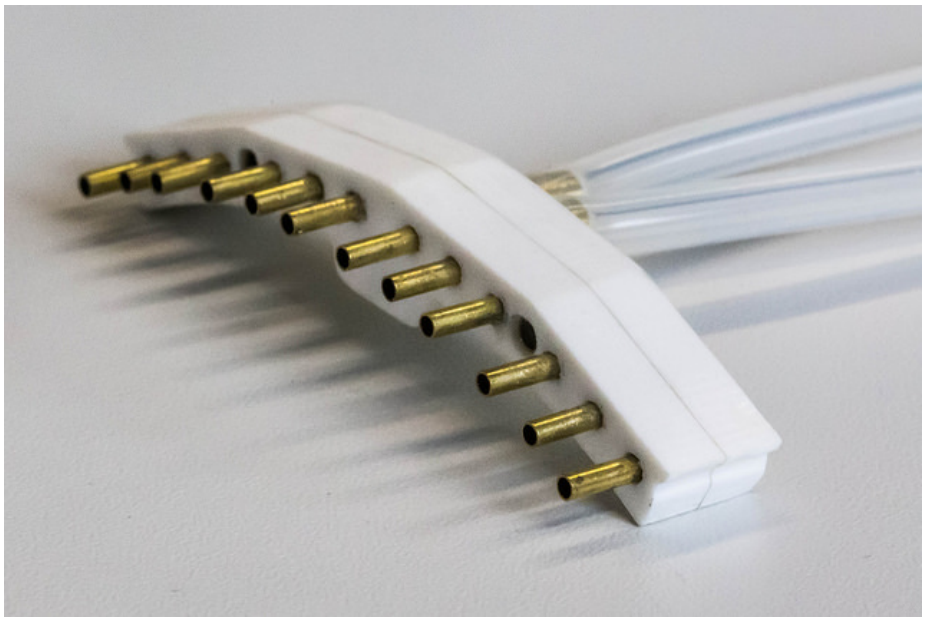

Figure 5.33: *Hardware for distribution of helium to the outlets in the module endpieces*

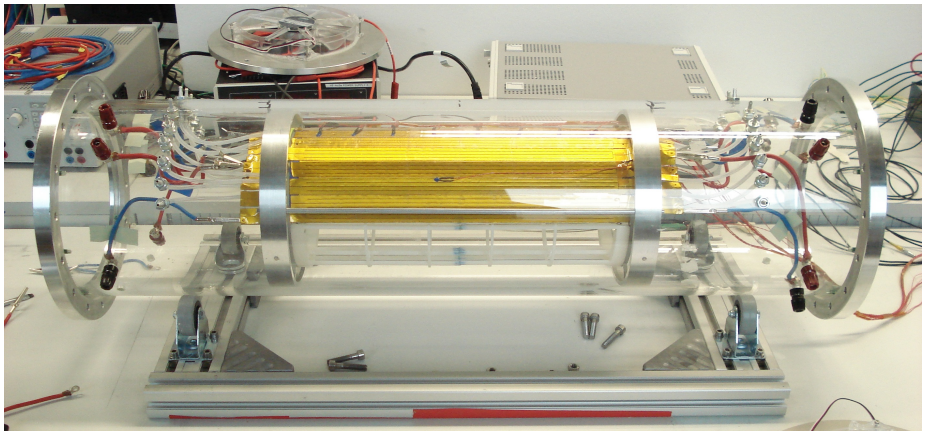

Figure 5.34: *Detector model consisting of heatable module prototypes placed in the flow channel*

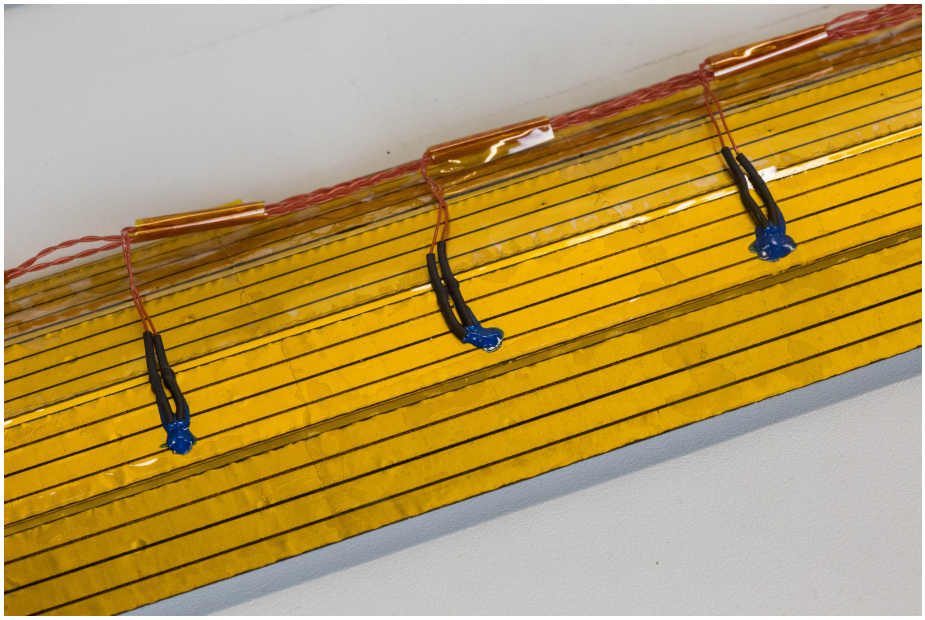

Figure 5.35: *Heatable module prototype with temperature sensors*

Local Helium Flow Velocity

In this section, an estimation of the required helium flow velocity inside the cooling channels is presented. It is assumed that, in equilibrium $\Delta T_{max} = 50°\mathrm{C}$, and that the temperature difference between the helium entering a fold and the outgoing helium is accordingly $\Delta T_{He} = 50\,°\mathrm{C}$. In general, for the specific heat capacity c_{He} one has

$$c_{He} = \frac{\Delta E}{m_{He} \cdot \Delta T_{He}} \tag{5.42}$$

where ΔE is the heat load. Reordering and dividing both sides by the time t gives

$$\frac{m_{He}}{t} = \frac{P}{c_{He} \cdot \Delta T_{He}} \tag{5.43}$$

with the heating power $P = \frac{Q}{t}$. The mass flow rate on the left hand side can be converted into the corresponding volume flow Q_{He} by deviding by the helium desity ρ_{He}. With $v_{local} = \frac{V_{He}}{A_c}$, where A_c is the cross-section area of a channel, one finally gets

$$v_{local} = \frac{P}{A_c \cdot \rho_{He} \cdot c_{He} \cdot \Delta T_{He}} \tag{5.44}$$

P is assumed to be the heating power of one heating stripe, since there is one fold per stripe on a module. By inserting the values

- $P = 1.8\,\mathrm{cm} \cdot 37\,\mathrm{cm} \cdot 150\,\frac{\mathrm{mW}}{\mathrm{cm}^2}$
- $c_{He} = 5193\,\frac{\mathrm{J}}{\mathrm{kgK}}$
- $\rho_{He} = 0.17\,\frac{\mathrm{kg}}{\mathrm{m}^3}$
- $A_c = 10\,\mathrm{mm}^2$

one gets $v_{local} \approx 23\,\frac{\mathrm{m}}{\mathrm{s}}$.
Therefore, for the cooling tests discussed in the following, the local flow velocity was set to approximately $20\,\frac{\mathrm{m}}{\mathrm{s}}$. This was done by adjusting the pressure reducer on the helium bottle while measuring the volume flow Q with a float-type flowmeter. The latter was placed in front of where the hose conveying the local flow enters the helium container. Assuming incompressible flow, the flow velocity v_{local} in the channels is given by

$$v_{local} = \frac{Q}{n \cdot A_c} \tag{5.45}$$

where n is the number of channels that the flow is distributed to.
The float-type flowmeter is calibrated for helium at $T = 20\,°\mathrm{C}$ and overpressure $\Delta p = 1\,\mathrm{bar}$. It is operated with helium at $T = 20\,°\mathrm{C}$, but at different pressures to vary the flow velocity. If the operating pressure p_{op} does not equal the pressure p_{cal}, at which the flowmeter was calibrated, a correction factor has to be applied to obtain the correct volume flow rate:

$$Q_{op} = Q_{cal} \cdot \sqrt{\frac{p_{cal}}{p_{op}}} \tag{5.46}$$

where p is the absolute pressure. The derivation of this correction factor can be found in Appendix A. The operating pressure was measured directly behind the flowmeter. For the measurements discussed below, values between $\Delta p = 0.5\,\text{bar}$ and $\Delta p = 1.7\,\text{bar}$ were obtained. For the measurement of Q_{cal}, a 4 % error is assumed, and for the correction factor a 3 % error. This yields an error on v_{local} of 5 %.

Results of the Cooling Tests with Heatable Module Prototypes

The first tests were performed with only one module prototype representing a cutout of layer 4. A measurement was carried out without heating the module to check if the temperature of the helium entering the local cooling system equals the environmental temperature T_0 of 20 °C. The results are shown in figure 5.36.

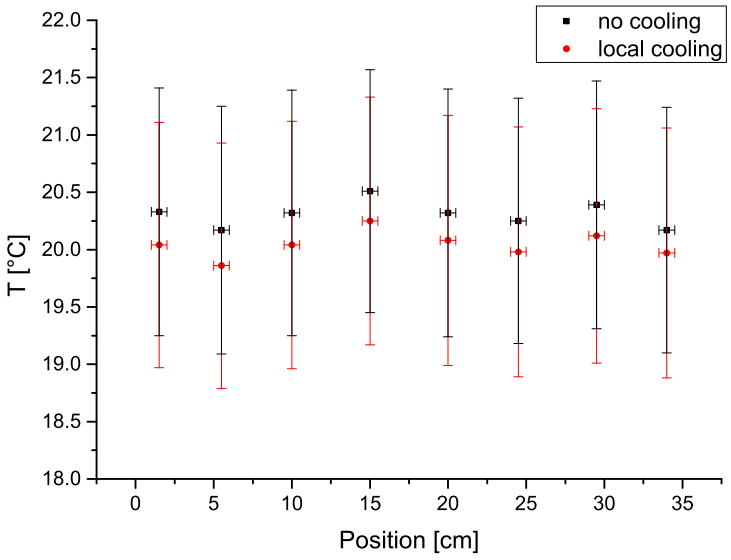

Figure 5.36: *Temperature profiles without heating, without global cooling, but with local cooling*

After switching on the local helium flow, the temperature was measured to be around 0.3 °C lower than without helium flow. This discrepancy is considered to be negligible, given the error bars, which are mostly given by the calibration error.
In the next step, the heating power was set to $P/A = 150\,\text{mW/cm}^2$, which corresponds to a total power of $P = 40\,\text{W}$. The local flow velocity was set to $(29 \pm 2)\,\frac{\text{m}}{\text{s}}$. Figure 5.37 compares the temperature profiles on the module prototype for global cooling only and with additional local cooling. It can be seen that additional local cooling improves the cooling performance significantly. A second module prototype was mounted directly underneath the first one to represent layer 3. A series of six measurements with varying parameters was carried out with this setup. The parameters for each measurement are summa-

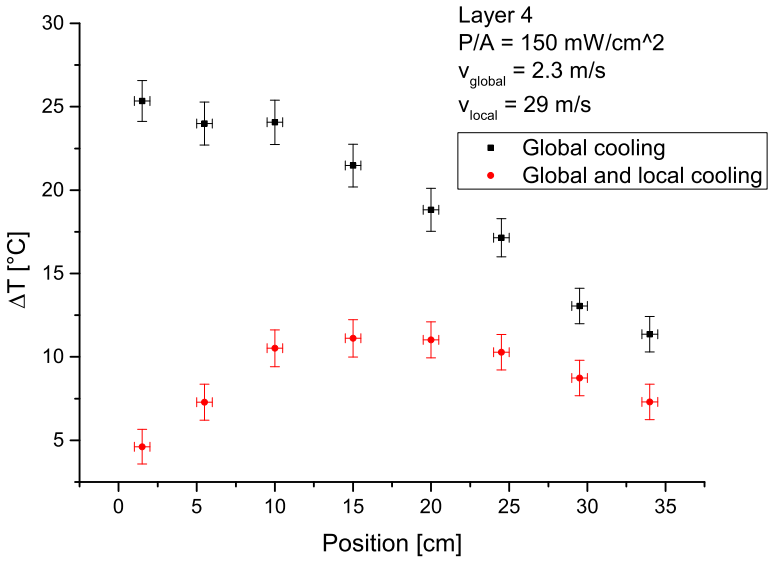

Figure 5.37: *Comparison of the temperature profiles with and without local cooling for only one module prototype at $P/A = 150\,mW/cm^2$*

rized in table 5.5. The resulting temperature profiles are shown in figure 5.38. Since the measurements for layer 3 and layer 4 were done simultaneously, there are only four measuring points per layer[5].

measurement	P/A [mW/cm^2]	v_{global} [m/s]	v_{local} [m/s]
1	150	2.3 ± 0.2	0
2	150	2.3 ± 0.2	20 ± 1
3	150	1.2 ± 0.1	0
4	150	1.2 ± 0.1	20 ± 1
5	250	2.3 ± 0.2	0
6	250	2.3 ± 0.2	20 ± 1

Table 5.5: *Parameters for experimental tests of local cooling with two heatable module prototypes*

In case, the power consumption of the MuPix chips is higher than expected, further tests were performed with higher heating powers of $P/A = 400\,\mathrm{mW/cm^2}$ and $P/A = 750\,\mathrm{mW/cm^2}$.
For the test with $P/A = 400\,\mathrm{mW/cm^2}$, the two module prototypes were cooled with a global flow of $v_{global} = (2.5 \pm 0.2)\,\frac{\mathrm{m}}{\mathrm{s}}$ and a local flow of $v_{local} = (20 \pm 1)\,\frac{\mathrm{m}}{\mathrm{s}}$. The resulting temperature profile is shown in figure 5.39. The peak temperature on the layer 3 module is approximately 43 °C. On the layer 4 module it is approximately 52 °C, i.e. 9 °C higher. This is still well below the upper limit of the MuPix temperature operating range of 70 °C. For the measurement with

[5]The stable current source for the Pt1000 sensors has only ten channels.

750 mW/cm^2, only the layer 4 module was heated (resulting in a total heating power of $P = 200$ W). Otherwise, the total heating power would have been too high to cool it away with the water cooling system for the helium container (see section 5.3.6). The module was cooled with a global flow of $v_{global} = (2.5 \pm 0.2)\ \frac{\mathrm{m}}{\mathrm{s}}$ and a local flow of $v_{local} = (25 \pm 2)\ \frac{\mathrm{m}}{\mathrm{s}}$. The resulting temperature profile is shown in figure 5.40. The peak temperature of approximately 63 °C is also still below 70 °C, but one has to keep in mind that this is only for one single module prototype. For the full cylindrical double layer and more than one detector station, a heat dissipation of 750 mW/cm^2 could probably not be cooled away with the planned cooling system.

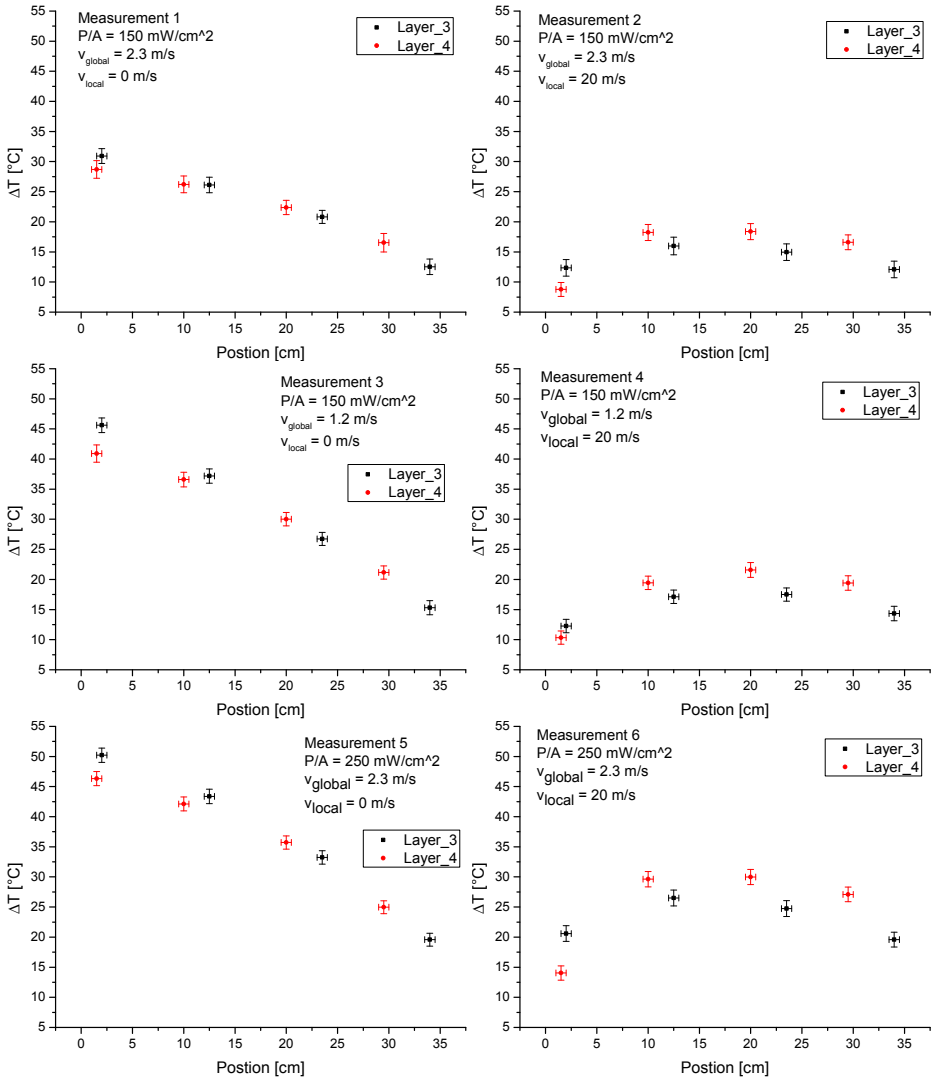

(a) without local cooling *(b) with local cooling*

Figure 5.38: *Temperature profiles for cooling tests with one layer 3 module and one layer 4 module*

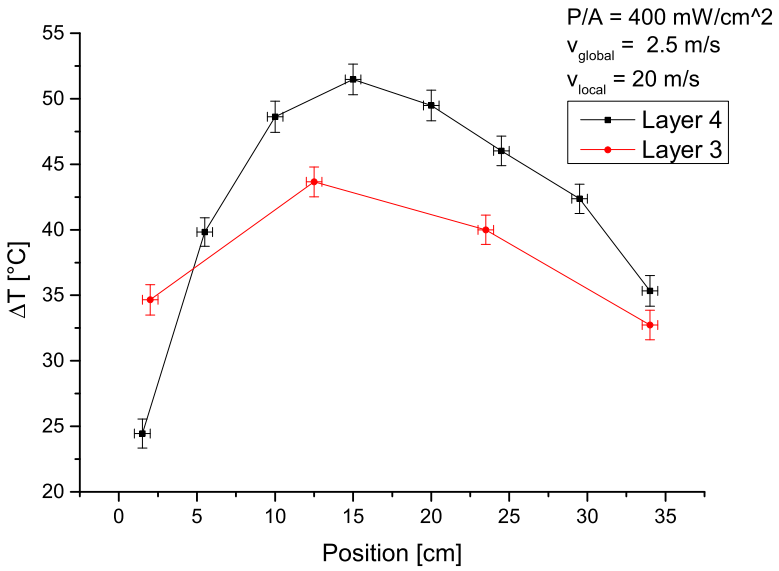

Figure 5.39: *Temperature profiles of layers 3 and 4 at* $P/A = 400\,mW/cm^2$ *with* $v_{global} = (2.5 \pm 0.2)\,\frac{m}{s}$ *and* $v_{local} = (20 \pm 1)\,\frac{m}{s}$

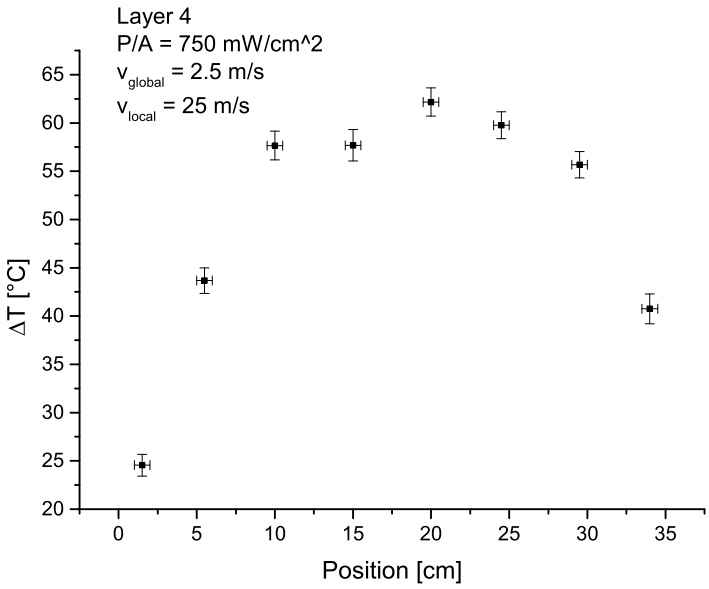

Figure 5.40: *Temperature profile of layer 4 at* $P/A = 750\,mW/cm^2$ *for layer 4 module prototype only with* $v_{global} = (2.5 \pm 0.2)\,\frac{m}{s}$ *and* $v_{local} = (25 \pm 1)\,\frac{m}{s}$

5.4 CFD Simulations

The theoretical treament of heat transfer by convection is very complex, even for rather simple geometries, as it is shown in section 5.1. To still be able to make theoretical predictions about the cooling of the Mu3e detector, computational fluid dynamics (CFD) simulations were carried out. They were performed with Autodesk® Simulation CFD.
In a first step, the software was tested and its accuracy was verified by performimg simulations according to the experimental cooling tests discussed in sections 5.3.5 to 5.3.7. After that, the goal has been to develop a simulation of the cooling of the full Mu3e detector that goes beyond the scope of possible experimental cooling tests in terms of size and detail of the used detector model. Another advantage of simulations is that new design iterations can be tested without the need of producing new physical prototypes for each step.

At first, the cooling of the full-scale model of layers 3 and 4 of one detector station in the flow channel, as described in section 5.3.5, was simulated.
In general, to successfully perform CFD simulations, it is often required to simplify the geometry under consideration. In this case, in contrast to the physical model, the support frame and all electrical connectors were neglected. Furthermore, the detector layers consist of polygons with 60 sides instead of cylinder barrels. The drawing of the model is shown in figure 5.41.

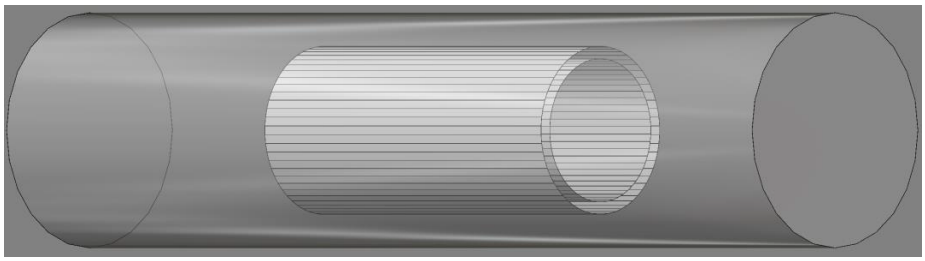

Figure 5.41: *Drawing of the geometry for the simulation of the cooling of the full outer double layer of one detector station [27]*

The detector layers are set to consist of 50 µm thin aluminium on 50 µm Kapton® polyimide film. The flow channel is represented by an acrylic glass tube with open ends. The inside of the flow channel was filled with air and helium, respectively. The boundary conditions were

- no-slip ($\vec{v} = \vec{0}$) on all walls
- uniform heat production in the aluminum corresponding to $100\,\mathrm{mW/cm^2}$ and $150\,\mathrm{mW/cm^2}$, respectively
- constant flow velocity (directed inwards, v ranging from 0.5 to 10 $\frac{\mathrm{m}}{\mathrm{s}}$ in different runs) and constant temperature $T = 20\,^{\circ}\mathrm{C}$ at one end of the flow channel
- zero overpressure at the opposite end of the flow channel to define an outlet

Figure 5.42 illustrates the results for $P/A = 150\,\mathrm{mW/cm^2}$ and $v = 3\,\frac{\mathrm{m}}{\mathrm{s}}$ for cooling with air and helium, respectively. It should be noted that the absolute temperature T is plotted, not ΔT.

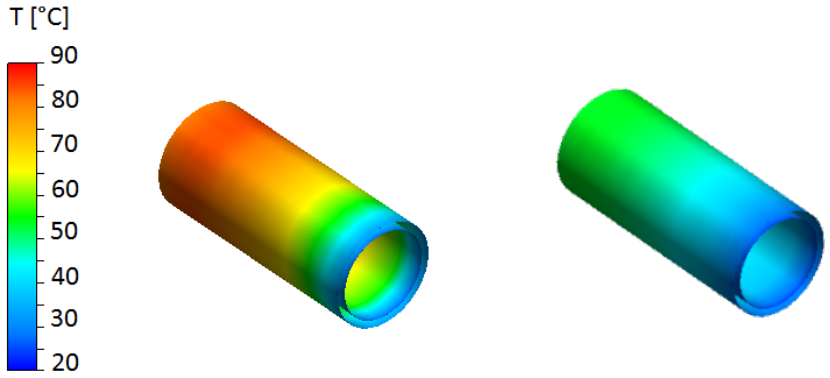

(a) Air *(b) Helium*

Figure 5.42: *Results of the simulation of the cooling of detector layers 3 and 4 of one station for* $P/A = 150\,mW/cm^2$ *and* $v = 3.0\,\frac{m}{s}$

To compare the measured and the simulated results, temperature profiles were plotted. As an example, figure 5.43 shows the profiles for air cooling at $P/A = 150\,\mathrm{mW/cm^2}$ for different flow velocities v.

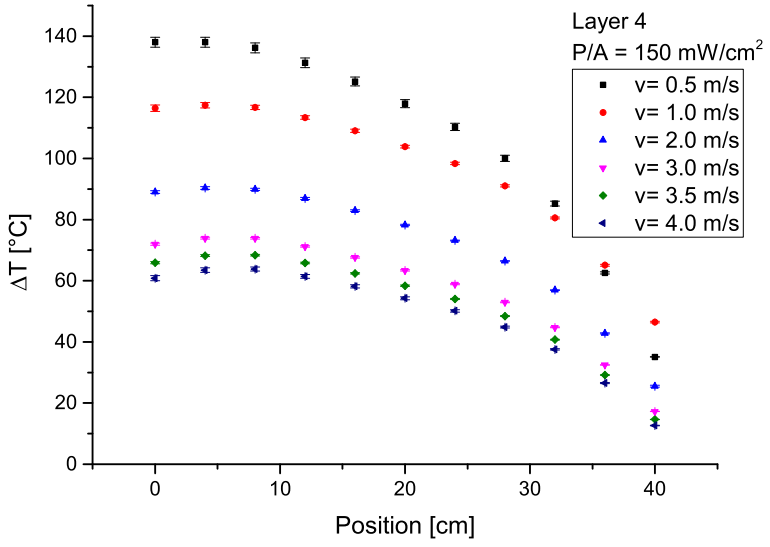

Figure 5.43: *Simulated temperature profiles for air cooling*

For direct comparison, figure 5.44 shows the simulated and the measured profile for $P/A = 150\,mW/cm^2$ and $v = 3.0\,\frac{m}{s}$.

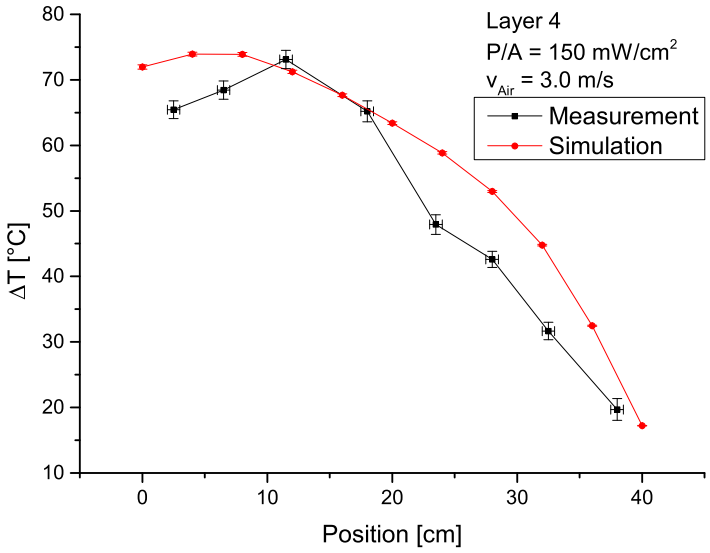

Figure 5.44: *Comparison of a measured and a simulated temperature profile*

Considering the geometrical simplifications that were made for the simulation, the results are in good agreement. One notable feature is the decrease of ΔT at the rear end of the model, which is observable in both the simulation and the measurement, although for the latter, it is more distinct. Here, it could be explained with the fact that, at the according position, the heating foils are in thermal contact with the aluminum endring of the detector model, which probably enhances the heat dissipation. In case of the simulation, where there is no endring, it is not known if this is an artefact of the software or an actual physical effect. It could be an edge effect caused by heat conduction inside the heating foil or an effect due to turbulences.
In figure 5.45, the simulated results for ΔT_{max} on both layers are plotted against v for helium cooling at $P/A = 150\,\mathrm{mW/cm^2}$. One can see that, for small flow velocities ($v \lesssim 2\,\frac{\mathrm{m}}{\mathrm{s}}$), ΔT_{max} is larger on layer 3 than on layer 4, whereas for $v \gtrsim 2\,\frac{\mathrm{m}}{\mathrm{s}}$, it is the other way around. But overall, the difference between the two layers is small.
Figure 5.46 shows ΔT_{max} plotted against v for simulations and measurements with air and with helium for $P/A = 100\,\mathrm{mW/cm^2}$. Considering again the simplifications in the geometry that was used in the simulation, as well as the method that the helium flow velocity was determined with in the experiment (see section 5.3.4), the simulated and measured results are in good agreement. In this plot, one should also note that there is a flow velocity v_c ($\approx 5\,\frac{\mathrm{m}}{\mathrm{s}}$), above which the gradient of $\Delta T_{max}(v)$ becomes small. For more than one detector station, this v_c might get larger. However, when determining the optimal flow velocity for the global flow, one should identify the according v_c.

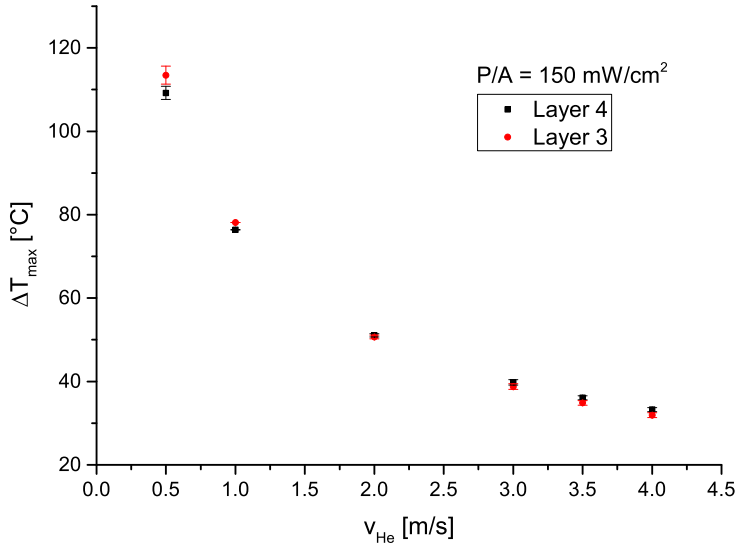

Figure 5.45: *Simulated ΔT_{max} plotted against helium flow velocity v for layers 3 and 4*

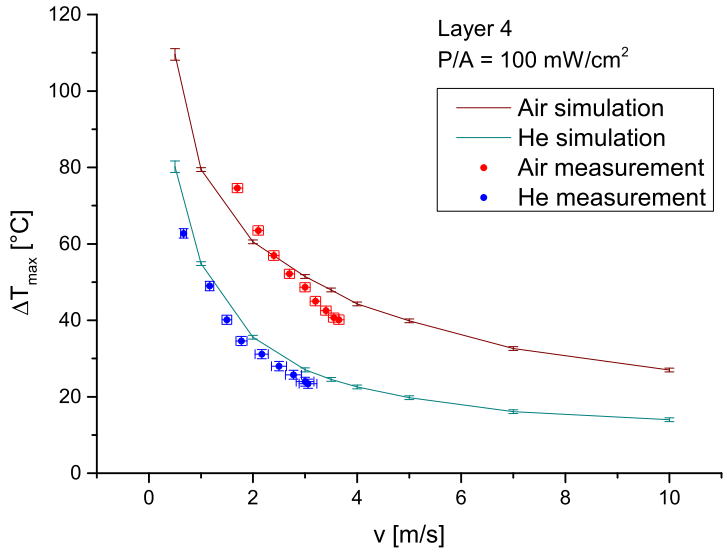

Figure 5.46: *ΔT_{max} plotted against flow velocity v for simulations and measurements with air and helium at $P/A = 100\,mW/cm^2$*

Simulations with Local Cooling

This section is based on simulations carried out by Yanwing Ng [35].
To perform simulations that include additional local cooling, the model shown in figure 5.47 was used. It is similar to the original design of layers 3 and 4 of one detector station, with only few modifications that had to be made in order to successfully create volume and surface meshes. First, the 1 mm overlap of the silicon sensors was neglected. Second, the original helium distribution system was replaced by rectangular pipes.

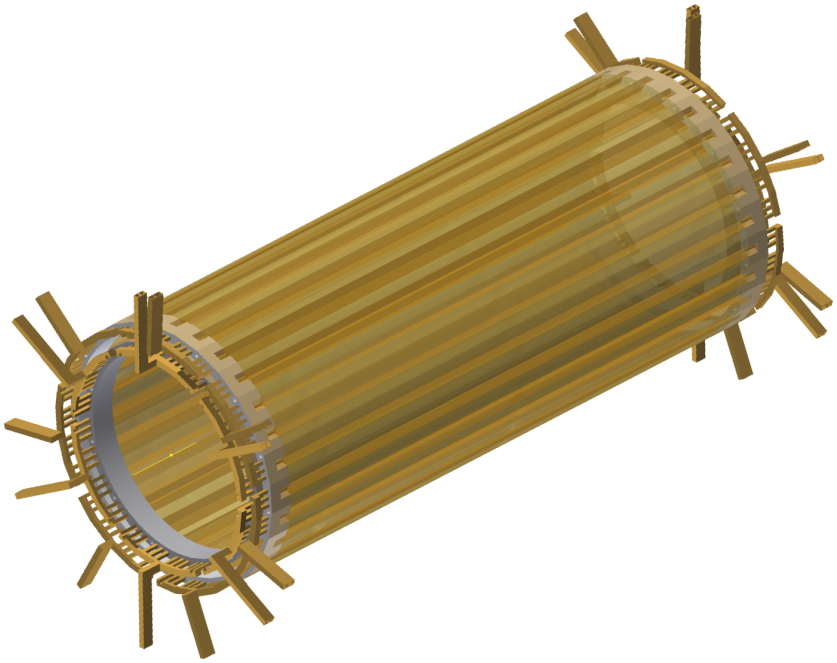

Figure 5.47: *CAD model used for simulations including local cooling*

The simulations discussed in the following were all carried out with a heating power of $P/A = 400\,\mathrm{mW/cm^2}$, a temperature of the incoming helium of 20 °C, a global helium flow with $v_{global} = 4\,\frac{\mathrm{m}}{\mathrm{s}}$, and an oppositely directed local helium flow with $v_{local} \approx 20\,\frac{\mathrm{m}}{\mathrm{s}}$. All figures are oriented such that the global flow is coming from the right.
Figure 5.48 shows the distribution of the absolute value of the helium flow velocity in a plane parallel to the beam axis. The flow velocity outside of layer 4 and in the center of the model ranges from 4 to $10\,\frac{\mathrm{m}}{\mathrm{s}}$. Inside the cooling channels it reaches up to $30\,\frac{\mathrm{m}}{\mathrm{s}}$, but on average it is below that. Inside the gap between the two layers, there is almost no flow. This is an issue, but it should be solvable by supplying additional helium in the same way as the local flow, only not inside the cooling channels, i.e. this additional flow has to be applied in the direction of the global flow [35].
Figure 5.49 is a similar plot, but for the overpressure. In the pipes that distribute the helium, a maximum overpressure of about 0.6 bar is required to establish the above flow velocities. Inside the cooling channels, the overpressure is constant at approximately 0.3 bar.

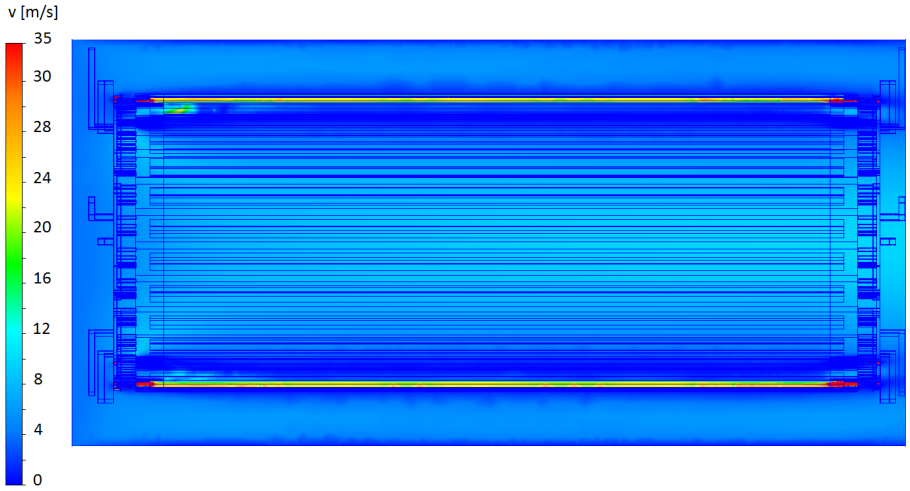

Figure 5.48: *Simulated distribution of the helium flow velocity in a plane parallel to the beam axis for* $v_{global} = 4\ \frac{m}{s}$ *and* $v_{local} \approx 20\ \frac{m}{s}$

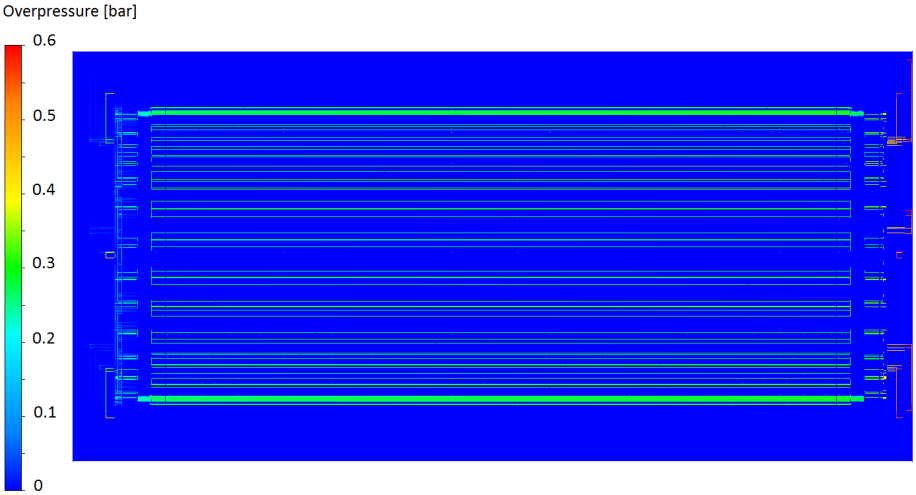

Figure 5.49: *Simulated distribution of overpressure in a plane parallel to the beam axis for* $v_{global} = 4\ \frac{m}{s}$ *and* $v_{local} \approx 20\ \frac{m}{s}$

Figure 5.50 shows the temperature distribution on the model. It should be noted that the absolute temerature according to an incoming helium temperature of 20 °C is plotted. The maximum temperature of approximately 61 °C corresponds to a ΔT_{max} of 41 °C.

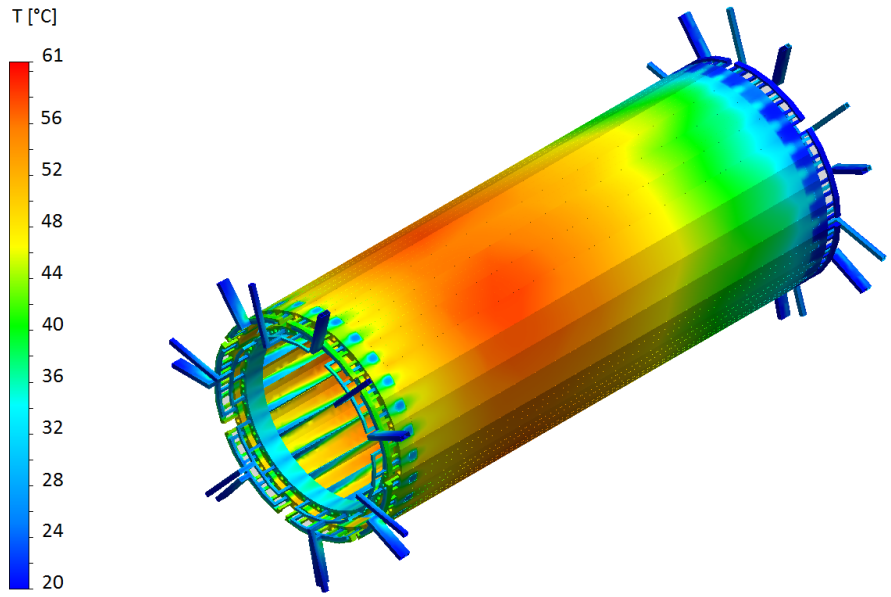

Figure 5.50: *Temperature results of the simulation including local cooling for one station,* $P/A = 400\,mW/cm^2$, $v_{global} = 4\,\frac{m}{s}$, *and* $v_{local} \approx 20\,\frac{m}{s}$

Figure 5.51 shows the results for a simulation of two stations. Both stations are cooled by the same global flow, but the local flow is supplied to each station separately. The maximum temperature corresponds to $\Delta T_{max} \approx 46\,°C$. It is only 5 °C higher than for a single station. In the marked region, layer 4 is masked, such that layer 3 becomes visible. In contrast to the experimental local cooling tests, for the simulations, where the full detector layers are taken into account and not only a cutout, the maximum temperature is observed on layer 3. It is about 3 °C higher than the maximum on layer 4. Besides that, the temperature distribution is similar for the two layers.
Finally, figure 5.52 shows the temperature results for the simulation including three detector stations. The according ΔT_{max} of 54 °C is still well below the upper limit of the MuPix temperature operating range of 70 °C.
Further simulations of the Mu3e cooling system are discussed in [35].

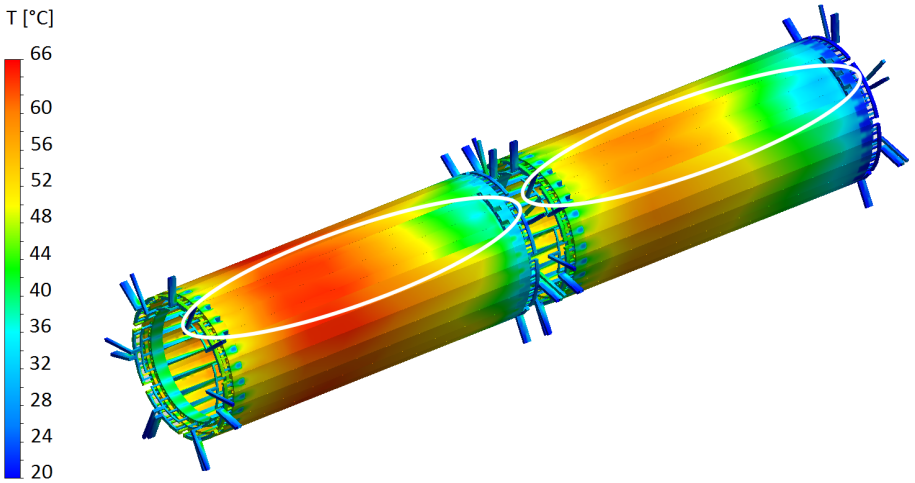

Figure 5.51: *Temperature results of the simulation including local cooling for two stations,* $P/A = 400\,mW/cm^2$, $v_{global} = 4\,\frac{m}{s}$, *and* $v_{local} \approx 20\,\frac{m}{s}$

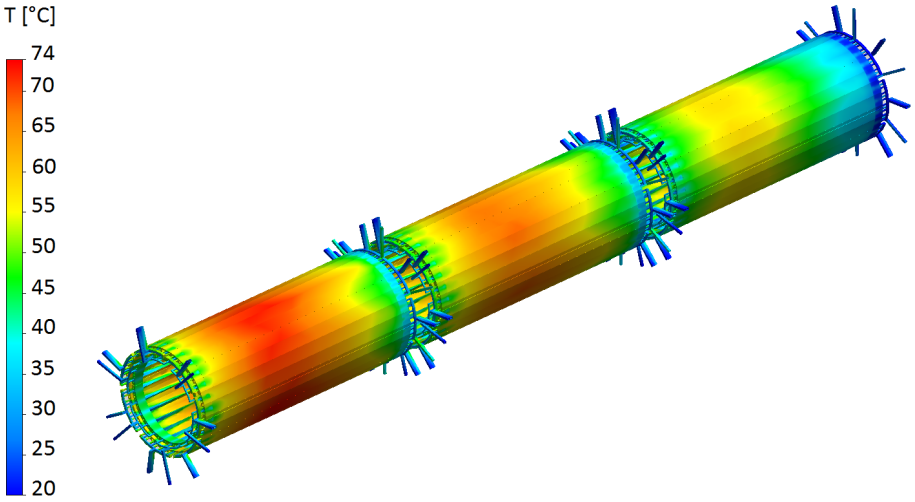

Figure 5.52: *Temperature results of the simulation including local cooling for three stations,* $P/A = 400\,mW/cm^2$, $v_{global} = 4\,\frac{m}{s}$, *and* $v_{local} \approx 20\,\frac{m}{s}$

5.5 Flow Induced Vibrations

Fluid flow in contact with a solid body can cause mechanical vibrations. There is a variety of different classes of flow induced vibrations. In many cases, instabilities occur, when the fluid flow velocity exceeds a critical value [36]. The investigation of the cooling concept for the Mu3e pixel detector showed that, especially for the local cooling system, relatively high helium flow velocities are required to achieve a sufficient cooling performance. Therefore, it needs to be investigated, if flow induced vibrations occur in the detector and if the corresponding amplitudes affect the momentum resolution. As a reference point, it is assumed that vibration amplitudes of the size $\lesssim 100\,\mu\text{m}$ (approximate scale of the pixel size) would not affect the momentum measurement significantly. Since the theoretical treatment of flow induced vibrations is very involved [37], experimental studies seem to be the faster and more reliable option. In the following, a strategy to measure the amplitude of mechanical oscillations with a Michelson interferometer is presented. While no actual results have been obtained yet, a proof of principle has already been achieved. The presented method has the advantages that it provides very high spatial resolution, it is contactless, and it does not require any calibration.

Michelson Interferometer

A Michelson interferometer allows for measuring relative changes in length by splitting a coherent light source in two and making it interfere with itself after the two wavefronts acquired a phase difference by travelling paths of different lengths. Figure 5.53 shows an according schematic.

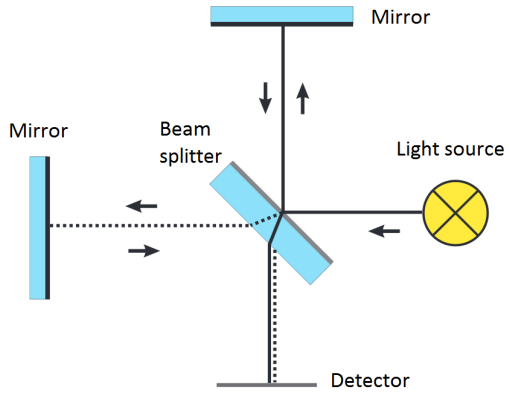

Figure 5.53: *Schematic of a Michelson interferometer [38]*

On the detector, an interference pattern is observable. If one mirror is moved in the direction parallel to the light path, for example, by half the wavelength $\frac{\lambda}{2}$ of the monochromatic light, an intensity minimum will be observable at the position of a former intensity maximum and vice versa. If the mirror moves by an unknown distance d, the latter can be determined simply by counting the number n of minima or maxima passing through a point on the detector during the movement. d is then given by $d = n\lambda$. The spatial resolution is given by

approximately $\frac{\lambda}{2}$.
To measure vibrations, one of the mirrors has to be exchanged with the vibrating object. In this case, d resembles the vibration amplitude. To resolve the vibration in time, a photodiode connected to an oscilloscope can be used as detector.

Test setup

A test setup was used to varify the above method of measuring vibration amplitudes. A loudspeaker was placed behind one of the mirrors to drive it with a sinusoidal sound wave. Figure 5.54 shows a photo of the test setup.

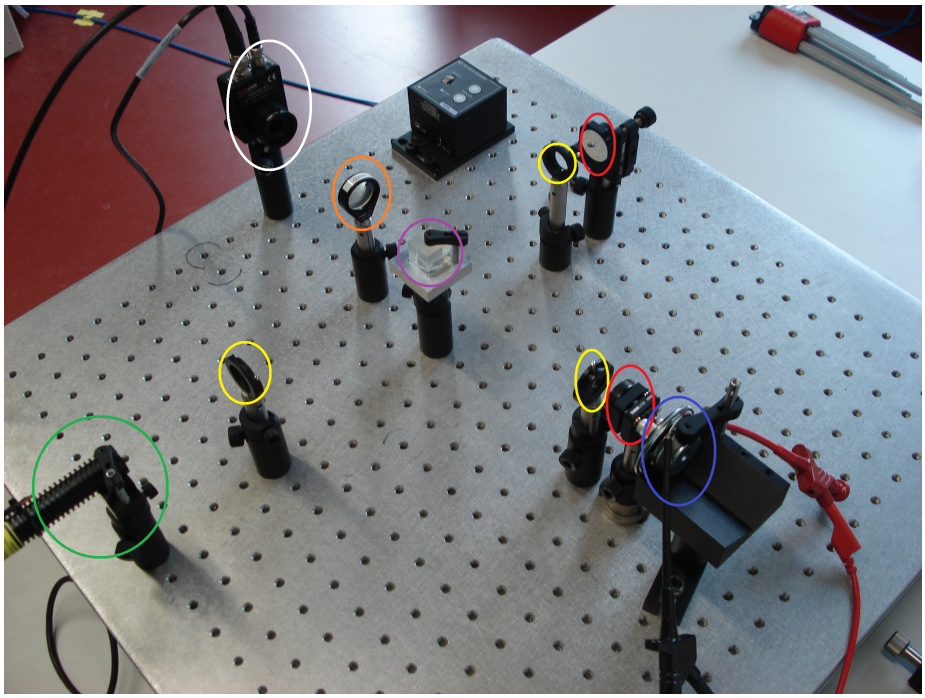

Figure 5.54: *Photo of the Michelson interferometer test setup showing the laser (green), three aperture plates (yellow), the beam splitter (purple), two mirrors (red), a lens (orange), the photodetector (white), and the loudspeaker (blue)*

The aperture plates were used to adjust the setup and the lens has the purpose of widening the beam, such that the photodiode only sees a small fraction of the interference pattern, i.e. only a maximum or a minimum. If the photodiode integrated over several intensity maxima, the measurement would not work.
The result of a test measurement is shown in figure 5.55.
The sine signal is produced by a function generator and transmitted to the oscilloscope and the loudspeaker. Its frequency is 504 Hz, which was found to be the resonance frequency of the mirror. The other signal (in yellow) is that of the photodiode. It shows four maxima and minima within one period. The laser wavelength is $\lambda_{laser} = 532\,\text{nm}$. Therefore, the vibration amplitude is approximately $\frac{4}{2} \cdot \lambda_{laser} \approx 1.1\,\mu\text{m}$. The uncertainty is below $\frac{1}{2} \cdot \lambda_{laser} = 266\,\text{nm}$.

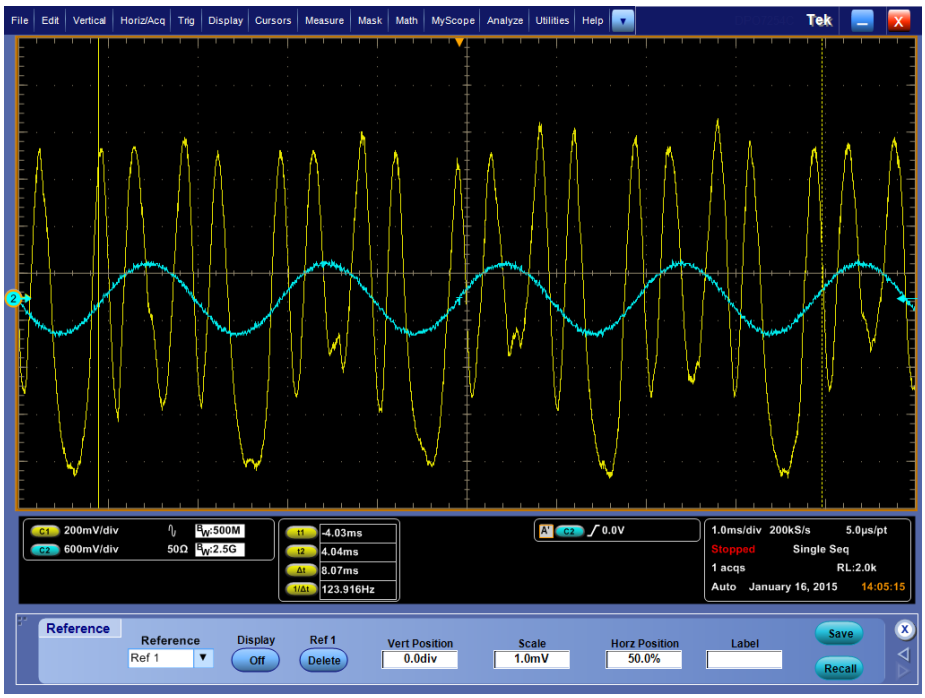

Figure 5.55: *Screenshot of oscilloscope during test measurement with Michelson interferometer showing the signal of the function generator (cyan) and the signal of the photodiode (yellow)*

Measuring Vibrations of a Tracker Module

There are several challenges in applying the above method to measure the flow induced vibrations of the Mu3e pixel detector. For a start, it is planned to replace the vibrating mirror by a single tracker module prototype, as described in section 5.3.7, and to apply the local cooling flow. Since the laser wavelength is different in helium and in air, the test has to be carried out with air flow or with helium flow inside a helium atmosphere. Another issue is that the reflection of the laser light on the module itself does not produce clean wavefronts. Therefore, a mirror has to be attached to it. One possibility would be to metallize one of the glass plates on the module with aluminum.

Chapter 6

Conclusions

The Mu3e experiment will search for the lepton flavor violating decay $\mu^+ \to e^+e^+e^-$ with a sensitivity for the branching ratio of 10^{-16}, which is four orders of magnitude better than in previous experiments. The decay is suppressed to unobservable levels in the Standard Model, but many New Physics models predict branching ratios higher than the aimed sensitivity. Therefore, a signal would be a clear sign of physics beyond the SM.
In order to reach the above sensitivity, backgrounds have to be suppressed below this level, which requires high momentum, vertex and time resolution. In the energy regime of the decay electrons (positrons), which is $E \lesssim 53\,\mathrm{MeV}$, the momentum and vertex resolution is limited by multiple Coulomb scattering in the detector material. This leads to the requirement of a very low material budget in the acceptance region. It can be met by the pixel tracker consisting of thin High-Voltage Monolithic Active Pixel Sensors, which can be thinned to 50 µm. HV-MAPS also include fast readout electronics, which is important considering the high muon decay rates necessary for the Mu3e experiment. The expected power consumption is approximately $250\,\mathrm{mW/cm^2}$.
The cooling system for the pixel detector must meet the requirement of a low material budget, which lead to the concept of cooling with gaseous helium. This concept has to be investigated.
In the context of this thesis, a heatable model of the outer double layer of the central pixel detector was produced and cooled with global flows of air and helium in a flow channel. The expected better cooling capabilities of helium compared to air could be varified and it was shown that, for a power consumption of $100\,\mathrm{mW/cm^2}$, cooling the outer double layer of the central pixel detector sufficiently ($T < 70\,^\circ\mathrm{C}$) would require only a global helium flow of approximately $1\,\frac{\mathrm{m}}{\mathrm{s}}$. The results of these experimental cooling tests could be confirmed by CFD simulations.
It is expected that, for cooling the full detector with a power consumption of $250\,\mathrm{mW/cm^2}$, a global helium flow is not sufficient. Therefore, a local cooling system had been designed, which makes use of cooling channels formed by prism shaped folds in the pixel tracker support structure. This system allows for distributing helium directly to individual parts of the detector and for cooling it from both sides simultaneously.
The local cooling system was tested experimentally, using heatable tracker module prototypes, and by performing CFD simulations.

The experimental tests show that the local cooling system can be realized and that it improves the cooling performance significantly. The tests were carried out with heatable tracker module prototypes. Local flow velocities up to $\approx 29\,\frac{\mathrm{m}}{\mathrm{s}}$ were tested. The modules stayed damage-free. A cutout of layers 3 and 4 consisting of two module prototypes was heated with powers of up to $P/A = 400\,\mathrm{mW/cm^2}$ and cooled with combinations of global helium flows with flow velocities v_{global} of about $2.5\,\frac{\mathrm{m}}{\mathrm{s}}$ and local helium flows with flow velocities v_{local} of the order of $20\,\frac{\mathrm{m}}{\mathrm{s}}$. For all tests, the peak temperature ΔT_{max} was well below $70\,^{\circ}\mathrm{C}$ on both layers. A test with a single module prototype, heated with $750\,\mathrm{mW/cm^2}$ and cooled with $v_{global} \approx 2.5\,\frac{\mathrm{m}}{\mathrm{s}}$ and $v_{local} \approx 25\,\frac{\mathrm{m}}{\mathrm{s}}$, resulted in a peak temperature $\Delta T_{max} \approx 63\,^{\circ}\mathrm{C}$. It is assumed that, for the full detector, a dissipated power of $750\,\mathrm{mW/cm^2}$ could not be cooled away with the proposed cooling system.
The CFD simulations including local cooling show that at least three detector stations with a power consumption of $400\,\mathrm{mW/cm^2}$ can be sufficiently cooled by combining global cooling with flow velocities of about $4\,\frac{\mathrm{m}}{\mathrm{s}}$ and local cooling with flow velocities of the order of $20\,\frac{\mathrm{m}}{\mathrm{s}}$.
It should be confirmed that no flow induced vibrations affecting the momentum resolution of the pixel tracker occur due to high local flow velocities. A strategy to measure the amplitudes of potential vibrations of a tracker module prototype is presented in this thesis.
Concerning further studies, it should be the goal to perform a CFD simulation that comes as close to the real experimental situation as possible. Parts that still need to be included are the beam pipe, the readout electronics inside the recurl stations, and the timing detector, which all block a relevant part of the global helium flow, and in case of the readout electronics, represent an additional heat source. Another heat source that has been neglected so far is the inner double layer of the pixel detector, which can only be cooled locally because it is not reached by the global flow.
The methods that were used, in the context of this thesis, to investigate the gaseous helium cooling of the pixel detector can also be applied for investigating the liquid beam pipe cooling, which is planned to be a complementary cooling system for the Mu3e experiment.

Appendix

Appendix A

Correction Factors for Float-type Flowmeters

Float-type flowmeters have to be calibrated. This happens under certain conditions (calibration conditions), i.e at a fixed pressure and temperature. They also have to be calibrated for a particular fluid. If they are operated at conditions that differ from the calibration conditions, the flow rate indicated by the flowmeter is not correct anymore. However, one can apply correction factors to obtain the true flow rate. In the following, a derivation of these correction factors is given.

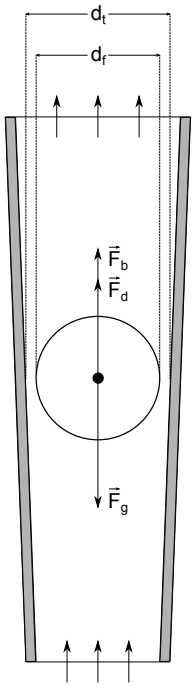

Figure A.1: *Schematic of a float-type flowmeter*

There are three forces acting on the float:

- Gravitational force $F_g = V_f \cdot \rho_f \cdot g$
- Buoyant force $F_b = V_f \cdot \rho_g \cdot g$
- Drag force $F_d = c_d \cdot A_f \cdot \rho_g \cdot \frac{v^2}{2}$

with

- float volume V_f
- float density ρ_f
- gravitational acceleration g
- gas density ρ_g
- drag coefficient c_d
- cross-section area of the float A_f
- flow velocity v

$\vec{F}_d$ and $\vec{F}_b$ are directed upwars, while $\vec{F}_g$ is directed downwards. Due to the tapered shape of the flowmeter tube, F_d depends on the height of the float in addition to the flow velocity. In the equilibrium state, one has

$$F_g = F_b + F_d \tag{A.1}$$

Inserting the above terms for the forces and reordering yields

$$v = \sqrt{\frac{2V_f \cdot g \cdot \rho_f}{c_d \cdot A_f}} \cdot \sqrt{\frac{1}{\rho_g}\left(1 - \frac{\rho_g}{\rho_f}\right)} \tag{A.2}$$

where the first term is considered independent of the operating conditions. Although c_d depends in principle on the viscosity, for float-type flowmeters, the viscosity dependence is usually assumed to be nigligible over a wide range. In the context of this thesis, the flowmeter has anyway been calibrated for the right measuring gas (helium). The volume flow rate Q is given by

$$Q = v \cdot \frac{\pi}{4}(d_t^2 - d_f^2) \tag{A.3}$$

where d_f and d_t are the diameters of the float and the flowmeter tube, respectively. For a fixed height of the float, i.e. for a fixed d_t, one gets the following relation by inserting (A.2) in (A.3):

$$Q \propto \sqrt{\frac{1}{\rho_g}\left(1 - \frac{\rho_g}{\rho_f}\right)} \tag{A.4}$$

In the case $\rho_f \gg \rho_g$, this becomes

$$Q \propto \sqrt{\frac{1}{\rho_g}} \tag{A.5}$$

In the following, the index of ρ_g is dropped, calibration conditions are denoted by *cal*, and operating conditions are denoted by *op*. It follows from (A.5) that

$$Q_{op} = Q_{cal} \cdot \sqrt{\frac{\rho_{cal}}{\rho_{op}}} \tag{A.6}$$

With the ideal gas equation $pV = nRT$ together with $\rho = \frac{nM}{V}$, where R is the ideal gas constant, n is the amount of substance, and M is the molar mass, one gets

$$\rho \propto \frac{p}{T} \tag{A.7}$$

and therefore

$$\rho_{op} = \rho_{cal} \cdot \frac{p_{op}}{p_{cal}} \cdot \frac{T_{cal}}{T_{op}} \tag{A.8}$$

Inserting (A.8) in (A.6) gives

$$Q_{op} = Q_{cal} \cdot \sqrt{\frac{p_{cal}}{p_{op}}} \cdot \sqrt{\frac{T_{op}}{T_{cal}}} \tag{A.9}$$

Appendix B

Data Acquisition Software

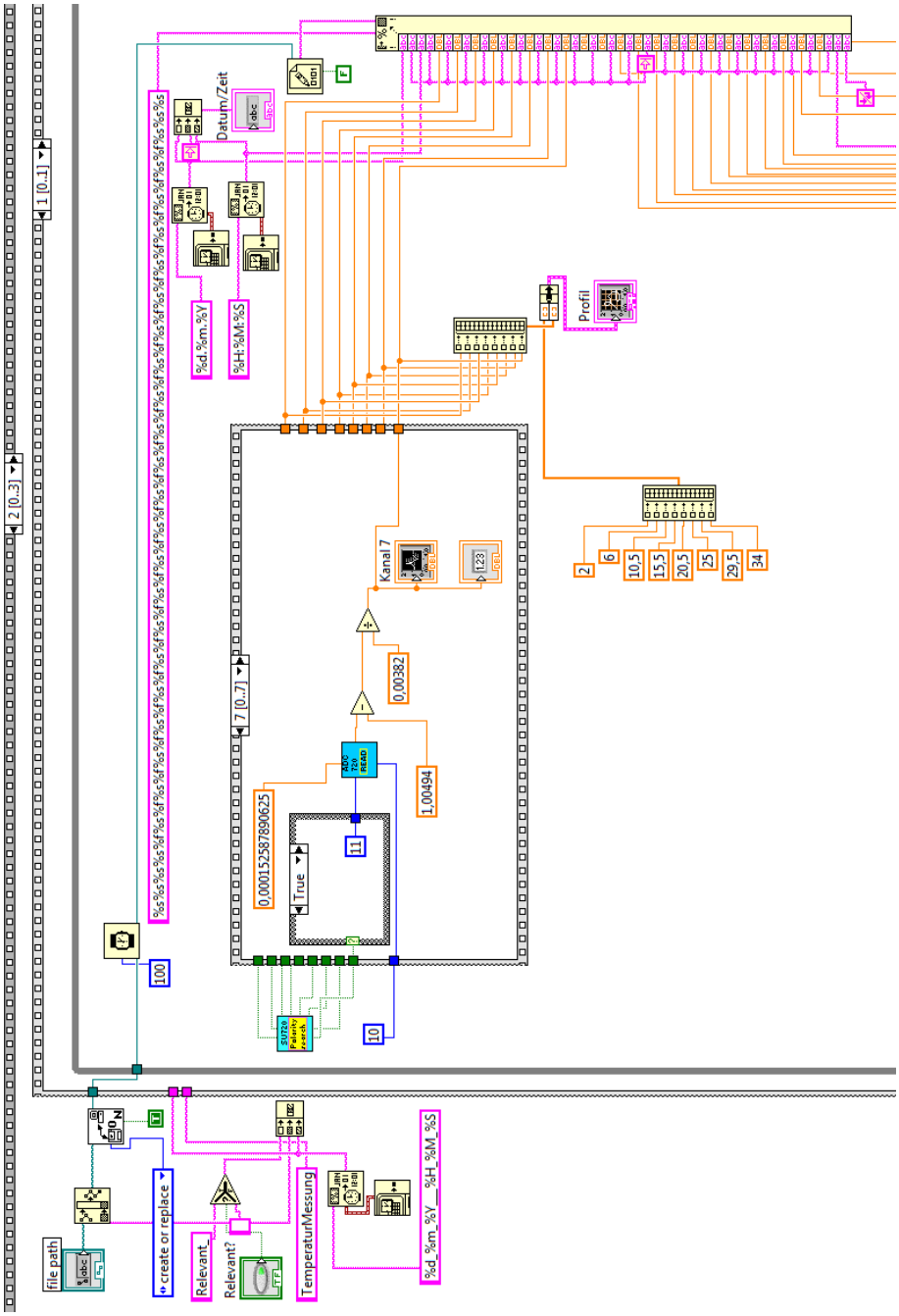

Figure B.1: *Excerpt from the temperature data readout program code implemented in LabVIEW™ software*

List of Figures

List of Tables

Bibliography

[1] N. Berger et al., [Mu3e Collaboration], *"Research Proposal for an Experiment to Search for the Decay $\mu \to eee$"*, 2013, arXiv:1301.6113 [physics.ins-det].

[2] Wikimedia Commons, *Standard Model of Elementary Particles*, retrieved December 2014.

[3] P. Higgs, *"Broken symmetries and the masses of gauge bosons"*, Phys. Rev. Lett. 13, 508, 1964.

[4] M. Kobayashi and T. Maskawa, *"CP-Violation in the Renormalizable Theory of Weak Interaction"*, Progr. Theor. Phys. 49 (2), 652-657, 1973.

[5] Y. Fukuda et al., [Super-Kamiokande Collaboration], *"Evidence for oscillation of atmospheric neutrinos"*, Phys. Rev. Lett. 81, 15621567, 1998, (arXiv:hep-ex/9807003).

[6] Q. R. Ahmad et al., [SNO Collaboration], *"Measurement of the charged current interactions produced by B-8 solar neutrinos at the Sudbury Neutrino Observatory"*, Phys. Rev. Lett. 87, 071301, 2001, (arXiv:nucl-ex/0106015).

[7] K. Eguchi et al., [KamLAND Collaboration], *"First Results from KamLAND: Evidence for Reactor Antineutrino Disappearance"*, Phys. Rev. Lett. 90, 021802, 2003, (arXiv:hep-ex/0212021).

[8] S.L. Glashow, J. Iliopoulos and L. Maiani, *"Weak Interactions with LeptonHadron Symmetry"*, Phys. Rev. D 2, 1285, 1970.

[9] R. M. Djilkibaev and R. V. Konoplich, *"Rare Muon Decay $\mu^+ \to e^+e^+e^-\nu_e\overline{\nu}_\mu$"*, Phys. Rev. D 79, 073004, 2009, arXiv:0812.1355 [hep-ph].

[10] I. Peric, *"A novel monolithic pixelated particle detector implemented in high-voltage CMOS technology"*, Nucl. Instrum. Meth. A582 (3), 876885, 2007.

[11] R. H. Bernstein and P. S. Cooper, *"Charged Lepton Flavor Violation: An Experimenter's Guide"*, Phys. Rep. 532 (2), 27-64, 2013, arXiv:1307.5787 [hep-ex].

[12] M. Frank and K. Huitu, *"Spontaneous R-Parity violation bounds"*, Phys. Rev. D 64, 095015, 2001, arXiv:hep-ph/0106004.

[13] Y. Kuno and Y. Okada, *"Muon Decay and Physics Beyond the Standard Model"*, Rev. Mod. Phys. 73, 151-202, 2001, arXiv:hep-ph/9909265.

[14] W. J. Marciano, T. Mori and J. M. Roney, *"Charged Lepton Flavor Violation Experiments"*, Annu. Rev. Nucl. Part. Sci. 58, 31541, 2008.

[15] J. Adam et al., [MEG Collaboration], *"New constraint on the existence of the $\mu^+ \to e^+\gamma$ decay"*, Phys. Rev. Lett. 110, 201801, 2013, arXiv:1303.0754 [hep-ex].

[16] U. Bellgardt et al., [SINDRUM Collaboration], *"Search for the Decay $\mu^+ \to e^+e^+e^-$"*, Nucl. Phys. B 299 1, 1-6, 1988.

[17] W. Bertl et al., [SINDRUM II Collaboration], *"A Search for $\mu - e$ conversion in muonic gold"*, Eur. Phys. J. C 47, 337346, 2006.

[18] R. Tschirhart, *"The Mu2e experiment at Fermilab"*, Nucl. Phys. B Proc. Suppl. 210-211, 245-248, 2011.

[19] Y. Kuno, *"Lepton flavor violation: Muon to electron conversion, COMET and PRISM/PRIME at J-PARC"*, PoS NUFACT08 111, 2008.

[20] Y. Amhis et al., [Heavy Flavor Averaging Group], *"Averages of b-hadron, c-hadron, and tau-lepton properties as of early 2012"*, 2012, arXiv:1207.1158 [hep-ex].

[21] S. Davidson, S. Lacroix and P. Verdier, *"LHC sensitivity to lepton flavour violating Z boson decays"*, 2012, arXiv:1207.4894 [hep-ph].

[22] K. Nakamura et al., *"Review of Particle Physics"*, J. Phys. G: Nucl. Part. Phys. 37 075021, 290, 2010.

[23] A. Damyanova, *"Development of a Scintillating Fibre Tracker/Time-of-Flight Detector with SiPM Readout for the Mu3e Experiment at PSI"*, Master thesis, University of Geneva, 2013.

[24] T. Harion et al., *"STiC - a mixed mode silicon photomultiplier readout ASIC for time-of-flight applications"*, JINST 9 C02003, 2014.

[25] R. Bellwied et al., *"The STAR Silicon Vertex Tracker: A large area Silicon Drift Detector"*, Nucl. Instr. Meth. Phys. Res. A 499 2, 640-651, 2003.

[26] M. Zimmermann, *"Cooling with Gaseous Helium for the Mu3e Experiment"*, Bachelor thesis, Institute of Physics, Heidelberg University, 2012.

[27] L. Huxold, *"Cooling of the Mu3e Pixel Detector"*, Bachelor thesis, Institute of Physics, Heidelberg University, 2014.

[28] H. Augustin, *"Characterization of a novel HV-MAPS Sensor with two Amplification Stages and first examination of thinned MuPix Sensors"*, Master thesis, Institute of Physics, Heidelberg University, 2014.

[29] R. Philipp, *"Characterisation of High Voltage Monolithic Active Pixel Sensors for the Mu3e Experiment"*, Master thesis, Institute of Physics, Heidelberg University, 2014.

[30] V. Angelov and E. Rubio, personal communication, Heidelberg, 2013.

[31] F. P. Incropera, D. P. DeWitt, T. L. Bergman and A. S. Lavine, *"Fundamentals of Heat and Mass Transfer"*, John Wiley & Sons, Inc., textbook, 2007, ISBN: 9780471457282.

[32] J. H. Lienhard IV and J. H. Lienhard V, *"A Heat Transfer Textbook"*, Phlogiston Press, textbook, 2003, ISBN: 9780971383524.

[33] J. Wagner, *"Physikalisches Anfängerpraktikum der Universität Heidelberg - Praktikum I, Versuch 26, Schallgeschwindigkeit"*, Practical course instructions, Heidelberg University, 2010.

[34] Wikimedia Commons, *Velocity and Temperature boundary layer similarity*, retrieved January 2015.

[35] Y. Ng, *"Finite Element Simulations of the Cooling System for the Mu3e Experiment" (preliminary title)*, Master thesis, Ernst-Abbe-Hochschule Jena, 2015.

[36] S. Kaneko et al., *"Flow-induced vibrations: classifications and lessons from practical experiences"*, Elsevier S&T Books, Academic Press, textbook, 2014, ISBN: 9780080983523.

[37] M. P. Païdoussis and P. Besancon, *"Dynamics of arrays of cylinders with internal and external axial flow"*, Journal of Sound and Vibration 76 (3), 361-379, 1981.

[38] J. Wagner, *"Physikalisches Anfängerpraktikum der Universität Heidelberg - Praktikum IIA, Versuch 232, Michelson-Interferometer"*, Practical course instructions, Heidelberg University, 2009.

Acknowledgements

I would like to express my gratitude to Prof. Dr. André Schöning for giving me the opportunity to work in the Mu3e group and for supervising my thesis.
I would like to thank Prof. Dr. Ulrich Uwer for surveying my thesis as second examiner.
I want to thank the whole Mu3e group for providing a very enjoyable work environment and their help whenever I needed it. I would especially like to thank Dr. Dirk Wieder for helping me in any way possible. Special thanks also go to Yanwing Ng, without whom the simulation part of this thesis would by far not have progressed as well as it did.
And I want to thank Dr. Jens Wagner, who I could also always go to for help.

Erklärung:

Ich versichere, dass ich diese Arbeit selbstständig verfasst habe und keine anderen als die angegebenen Quellen und Hilfsmittel benutzt habe.

Heidelberg, den 26.02.2015 .....